Tectonophysics 779 (2020) 228375

Contents lists available at ScienceDirect

Tectonophysics

journal homepage: www.elsevier.com/locate/tecto

Regional-scale polydiapirism predating the Neoarchean Yilgarn Orogeny

I. Zibra[a,b,*], Y. Lu[a,c], F. Clos[b], R.F. Weinberg[b], M. Peternell[d], M.T.D. Wingate[a,c], M. Prause[a], M. Schiller[e], R. Tilhac[f]

[a] Geological Survey of Western Australia, 100 Plain Street, 6004 East Perth, Western Australia, Australia
[b] School of Earth, Atmosphere and Environment, Monash University, Clayton, VIC 3800, Australia
[c] Centre for Exploration Targeting and Australian Research Council Centre of Excellence for Core to Crust Fluid Systems (CCFS), School of Earth Sciences, The University of Western Australia, Crawley, WA 6009, Australia
[d] Department of Earth Sciences, University of Gothenburg, Box 460, 405 30 Gothenburg, Sweden
[e] Eberhard Karls Universität Tübingen Geschwister-Scholl-Platz, 72074 Tübingen, Germany
[f] ARC Centre of Excellence for Core to Crust Fluid Systems (CCFS) and GEMOC, Department of Earth and Planetary Sciences, Macquarie University, Sydney, NSW 2109, Australia

ARTICLE INFO

Keywords:
Structural geology
Tectonics
Microstructures
Quartz crystallographic preferred orientation
Zircon isotopes

ABSTRACT

Gneiss domes occur in a wide variety of orogenic and anorogenic domains of the continental crust, and play a major role in lithosphere dynamics by allowing upwards transfer of heat and mass. They commonly contain a core of granites and/or migmatites, overlain by a mantle of lower-grade rocks. Evolutionary models of many gneiss domes are controversial.

Here we use new structural and zircon isotopic data to unravel the tectono-magmatic evolution of the Yalgoo dome and surroundings, at the margins of the Neoarchean Yilgarn Orogen, Western Australia. The study area includes at least seven granite–migmatite domes (5–70 km in average diameter), and several subdomes within the larger domes, all showing comparable structural features and age. In each dome, a concentric domal foliation is concordant with granite–greenstone contacts, bearing a radial, outward-plunging lineation. The bulk of the structures in each dome reflect magmatic flow, with pervasive subsolidus fabrics occurring only along the outer dome margins, and reflecting dome-up kinematics. Narrow greenstone keels pinched between domes and subdomes display vertical constriction, in an area regionally dominated by flattening along the steep sides of the deeply-eroded domes, and along the flat-laying dome roofs.

The regional structural pattern and the kinematics of the high-strain zones are best explained by sequential emplacement of nested diapirs, which delivered large volumes of granitic magma in a c. 20 Myr time-span. The dome-and-keel regional architecture and the internal structures of each dome resulted therefore from multiscale polydiapirism. These diapirs were later weakly overprinted by a tectonic fabric that developed during the Neoarchean Yilgarn Orogeny. The contrast between the Yalgoo region and the rest of the craton, which was strongly reworked by this orogeny, highlights the dichotomy of tectonic styles in Archean terranes, demonstrating that diapirism dominated in times of tectonic quiescence.

1. Introduction

Gneiss domes and gneiss dome systems (Eskola, 1948; Yin, 2004) are striking geological features that occur in a variety of geological settings, from Precambrian cratons to present-day active orogens (Little et al., 2011). They play a major role in lithosphere dynamics by allowing upwards transfer of heat and material, thus contributing to the stabilization of the continental crust (Whitney et al., 2004). Gneiss domes show domal foliation patterns, and commonly include granites, migmatites, and/or other high-grade metamorphic rocks in their cores, enveloped by a mantle of dominantly metasedimentary and metavolcanic, lower-grade rocks.

The literature offers a wide variety of mechanisms for dome formation, and evolutionary models of many gneiss domes are still controversial (Mareschal and West, 1980). Early field and conceptual studies emphasized the role of Rayleigh–Taylor instabilities and diapirism (Bouhallier et al., 1995; Cruden, 1988; Dixon, 1975; Jackson and Talbot, 1989; Ramberg, 1972; Weinberg and Podladchikov, 1995), stressing the role of lower-crustal viscous flow and density contrast in shaping upper crustal geometries and kinematics. Other contributions

* Corresponding author at: Geological Survey of Western Australia, 100 Plain Street, 6004 East Perth, Western Australia, Australia.
E-mail address: ivan.zibra@dmirs.wa.gov.au (I. Zibra).

https://doi.org/10.1016/j.tecto.2020.228375
Received 14 October 2019; Received in revised form 10 February 2020; Accepted 15 February 2020
Available online 19 February 2020

focused on the role of tectonic activity in the strong upper crust in triggering and/or influencing the pattern of lower-crustal flow (e.g. Lister and Davis, 1989). Gneiss domes have been related to orthogonal superposed folding (Ramsay, 1967), duplex development in thrust systems, décollement faults in extensional environments (forming metamorphic core complexes), and fold culminations in strike-slip systems (Yin, 2004 for a review). A variety of processes may have cooperated or competed in variable extent and/or at different stages of dome formation (Vanderhaeghe et al., 2011), so that a superficially simple domal architecture may in fact represent the end product of a complex tectono-magmatic and metamorphic evolution (François et al., 2014; Kruckenberg et al., 2011).

Different processes of dome formation should be associated with typical dome-scale finite strain patterns, and so structural analysis is a fundamental tool for unravelling their evolution. For example, gneiss domes formed by superposed folds should show patterns of planar and linear structures consistent with doubly-folded surfaces (Whitney et al., 2004). Syn-orogenic domes should exhibit lineation patterns concordant with regional-scale strain fields (Yin, 2004). In contrast, diapiric domes may be discordant to regional structures and show radial lineation arrangements, evidence of magmatic flow and systematic spatial variations in the shape of the finite strain ellipsoid (Bouhallier et al., 1995; Brun et al., 1981; Chardon et al., 1996; Dixon and Summers, 1983). Diapiric gneiss dome system may include polydiapirs, which consist of diapirs within diapirs (termed also nested diapirs, or subdomes), and/or of clusters of individual diapirs within a batholith (Stephansson, 1975). They can also form from multiple episodes of heat transfer over longer time periods (e.g. Van Kranendonk et al., 2004). Polydiapirism results from sequential or simultaneous multiwavelength gravitational instabilities, primarily triggered by vertical and lateral variations in density, viscosity and crustal thickness (Weinberg and Schmeling, 1992).

Gneiss domes are common in Archean granite–greenstone terranes (Whitney et al., 2004), where the dome-and-keel architecture commonly reflects tectonic activity dominated by body forces, with igneous diapirism assisted by greenstone sagduction (Bouhallier et al., 1995; Choukroune et al., 1997; Collins, 1989). In contrast, other Archean terranes, such as those composing the Yilgarn Craton (Western Australia) include linear, upright fold belts and crustal-scale shear zones juxtaposing ribbon-like domains (Calvert and Ludden, 1999; Cruden et al., 2006; Myers, 1995; Zibra et al., 2017). Such a structural grain is prominent in the central and eastern part of the craton, but is in striking contrast with the regional-scale dome-and-keel architecture exposed along the western margin of the Yilgarn Craton (Figs. 1 and 2). In this area, the Yalgoo dome was originally described as the result of superposed folds (Myers and Watkins, 1985). More recently, using structural data from a small portion of the core of the dome, Clos et al. (2019a) suggested that diapirism occurred prior to compressional orogenesis. However, the relationships between these local structures (at ~1–10 km-scale, documented by Clos et al. (2019a, 2019b)) and regional-scale structures associated with the dome-and-keel architecture are unknown, and the relative timing between magmatism, diapirism and deformation in the Yalgoo area is presently poorly constrained. In this contribution we use new regional-scale meso- and microstructural data, supported by new zircon Lu-Hf isotope data and the available geochronology data, to unravel the tectono-magmatic evolution of the broader Yalgoo region.

2. Geological setting

2.1. The Yilgarn Craton

The Youanmi Terrane forms most of the western half of the Archean Yilgarn Craton (Fig. 1a) and includes 3000–2720 Ma greenstones intruded by 2960–2600 Ma granitic rocks (Fig. 1b; Van Kranendonk et al., 2013). Greenstones developed on older continental crust (Ivanic et al., 2012) and mainly include mafic–ultramafic rocks associated with banded iron-formation (BIF), reflecting deep-marine environments (Klein, 2005), in a time span that was likely dominated by periods of lithospheric extension (Van Kranendonk et al., 2013; Smithies et al., 2018). Greenstone stratigraphy records a drastic change in depositional environment during the c. 2730 Ma onset of the Neoarchean Yilgarn Orogeny (Zibra et al., 2017), with the appearance of syntectonic clastic deposits above a regional-scale unconformity (Chen et al., 2003; Morris et al., 2007; Van Kranendonk et al., 2013). Granitic magmatism throughout the craton occurred nearly continuously for c. 200 Myr, before and during the Yilgarn Orogeny (Ivanic et al., 2012; Smithies et al., 2018).

Most of the ~800 km-wide Yilgarn Orogen Craton includes a series of east-dipping, crustal-scale shear zones (Drummond et al., 2000; van der Velden et al., 2006; Wilde et al., 1996; Zibra et al., 2014), juxtaposing domains with contrasting stratigraphy (Wyche et al., 2012). Some of these large-scale structures represent long-lived, transpressional shear zones that were active during the synorogenic emplacement of granite plutons (Zibra et al., 2014; Zibra et al., 2017). These shear zones are broadly north-striking and can be followed for hundreds of kilometres along strike (Fig. 1), and are flanked by north-striking, high-strain greenstone belts (Vearncombe, 1998).

2.2. The Yalgoo area

In the western portion of the Youanmi Terrane, the granite–greenstone terranes of the Yalgoo area (Figs. 1 and 2) define dome-and-keel patterns that closely resemble the archetypal map-scale pattern of the East Pilbara Terrane, one of the areas where the dome-and-keel architecture was first studied in detail (Collins, 1989).

Greenstones of the Yalgoo area mainly includes 2960–2760 Ma, ≥8 km-thick, mafic–ultramafic successions (Ivanic et al., 2015; Zibra et al., 2016), unconformably overlain by the 2–3 km-thick siliciclastic Mougooderra Formation (Figs. 1 and 2, and Supplementary file S1; Watkins and Hickman, 1990). Mudstone from the top of this sequence provided a 2758 ± 4 (Lu et al., 2016a) maximum depositional age, while a sandstone sampled near the base of the formation returned 2841–2792 Ma detrital zircons, typical of a greenstone source area (Lu et al., 2018a). The Mougooderra Formation occurs in the Yalgoo area only (Fig. 1), and is roughly coeval with the regionally-extensive, c. 2750 Ma BIF-bearing sequence of the Wilgie Mia Formation (Van Kranendonk et al., 2013). Granite plutons in the area cluster around four discrete age groups (Table 1). The Kynea Migmatite, whose tonalite protolith was emplaced at c. 2950 Ma into older greenstone slivers, is exposed in the core of Yalgoo and Gullewa domes (Fig. 2; Clos et al., 2019a; Zibra et al., 2016). Migmatites occur as rafts within the c. 2760–2750 Ma Goonetarra Granodiorite and other three roughly coeval, voluminous granite plutons that reflect a regional-scale event of crustal reworking (Clos et al., 2019b; Ivanic et al., 2012). The dome-and-keel architecture of the Yalgoo area is postdated by the c. 2700 Ma, synorogenic Lakeside pluton (Zibra et al., 2014), which was emplaced along a high-temperature shear zone named here Mulloo shear zone (Fig. 2), and by the post-orogenic, 2640–2600 Ma Bald Rock Supersuite (Van Kranendonk et al., 2013).

2.3. Previous work on the Yalgoo area

Regional mapping conducted by the Geological Survey of Western Australia (GSWA) in the early 1980s (1:250.000 scale) provided first-order constraints on the lithological and structural architecture of the study area, and led Myers and Watkins (1985) to interpret the dome-and-keel architecture of the Yalgoo area as a result of superposed fold generated during regional deformation. GSWA remapped the study area in more detail in recent years (Ivanic et al., 2015; Zibra et al., 2016), in conjunction with detailed structural studies in the core of the Yalgoo dome (Clos et al., 2019a; Fenwick, 2014). Here, Clos et al. (2019a)

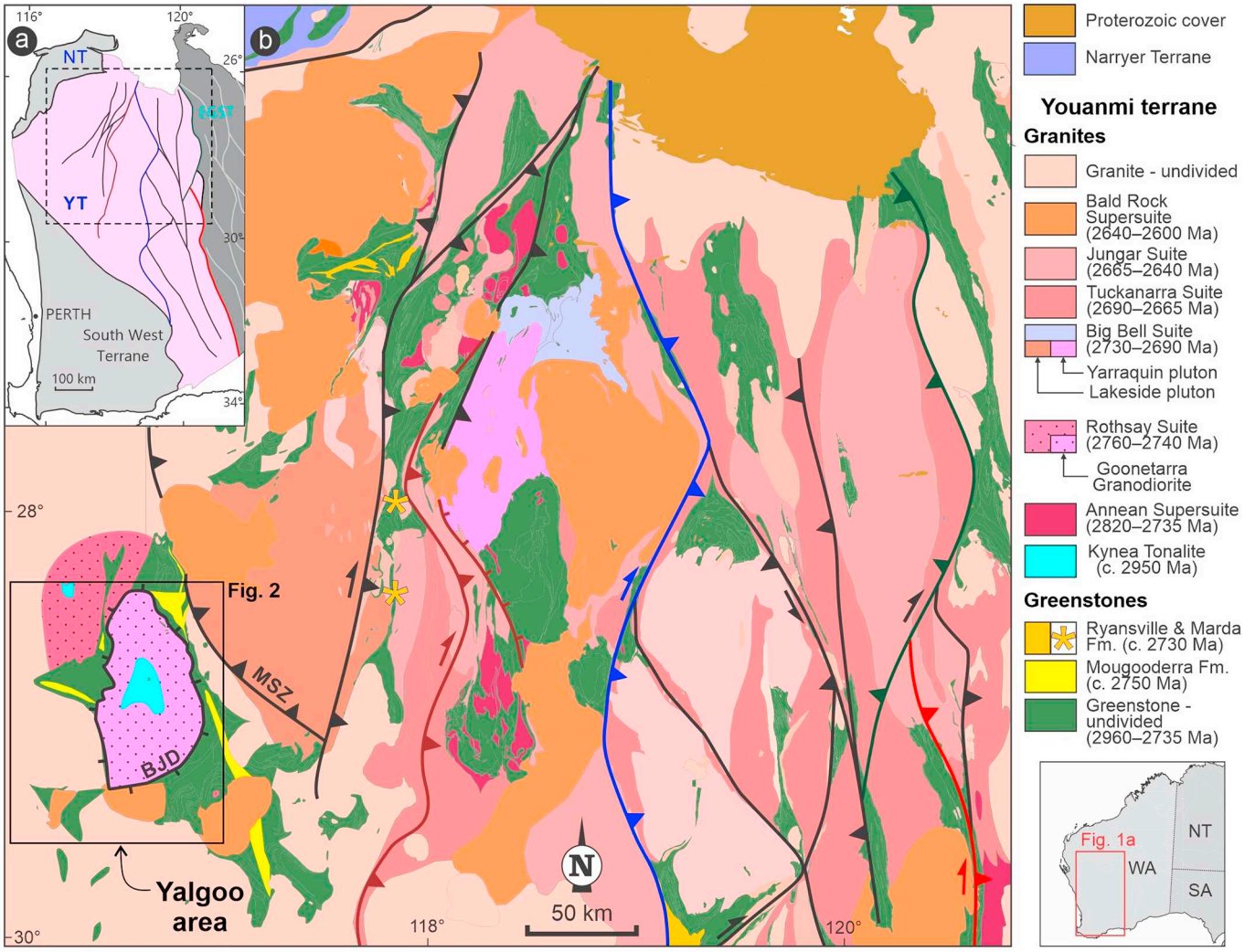

Fig. 1. (a) Simplified map of the western portion of the Yilgarn Craton, showing the main terranes (Cassidy et al., 2006) and the network of craton-scale shear zones. The rectangle shows the location of (b). Abbreviations: YT, Youanmi Terrane; NT, Narryer Terrane; EGST, Eastern Goldfields Superterrane. (b) Interpreted geological map of the central portion of the Youanmi Terrane. Map compilation is based on combined field and geophysical data. Abbreviations: BJD, Badja décollement; MT, Mulloo shear zone;

documented that dome-and-basin structures resulted from vertical sheath folds, inferred to represent the local expression of regional-scale structures associated with diapirism. Petrologic and geochemical data from the Kynea Migmatite are in fact consistent with diapirism, indicating water-fluxed melting and isothermal decompression from ~7 to ~4 kbar at ~750°C, during the emplacement of the Goonetarra Granodiorite (Clos et al., 2019b). Based on these data, Clos et al. (2019b) proposed that both granitic magmatism and the development of the dome-and-keel architecture in the Yalgoo dome represent the end product of prolonged mantle magmatism, which first developed a ≥8 km-thick greenstone pile overlying felsic crust; the consequent thermal anomaly in turn induced crustal magmatism and diapirism. In the core of the Yalgoo dome, diapirism-related structures recorded a minor overprint associated with the emplacement of granite dykes at c. 2700 Ma, during the Yilgarn Orogeny (Clos et al., 2019a). Based on regional geochemical data collected by GSWA, Nebel et al. (2018) suggested that the c. 300 Myr-long secular evolution of granite geochemistry in the Yalgoo area resulted from multiple melting events within long-lived lithospheric drips, triggered by mantle convection.

In summary, the core of the Yalgoo dome has provided local structural and petrologic data consistent with diapirism. In this context, we focus here on: (i) testing whether the small-scale structures described in the recent literature represent the local expression of large-scale diapirism; and (ii) constrain the relationship between the pre-orogenic dome-and-keel architecture and orogenic structures.

3. The domal fabric in the Yalgoo area

In the Yalgoo area we identify four large granitic domes (40–70 km in average diameter) and three smaller domes (5–10 km in average diameter, Fig. 2). The large domes are deeply eroded, locally down to their migmatitic cores (Yalgoo and Gullewa domes), they are commonly steep-sided, and separated by narrow greenstone keels, which are remnants of the heterogeneously-deformed supracrustal envelope. The smaller domes expose the flat-lying roofs of the granitic core (Mulgine dome) or are hidden under a domal-shaped greenstone cover only (Widdin and Rothsay domes, Figs. 2 and 3). We identify two distinct generations of fabrics: (i) domal fabric, homogeneously developed across the whole Yalgoo area; and (ii) the younger orogenic fabric, locally overprinting the domal fabric, along north-striking shear zones. The latter is examined in Section 4.

The domal fabric is defined by lithology distributions and a single foliation invariably parallel to lithological contacts. For the larger domes, this fabric developed at different metamorphic conditions in different domains, reflecting flow at suprasolidus conditions in the granite–migmatite cores, progressively grading to lower-temperature

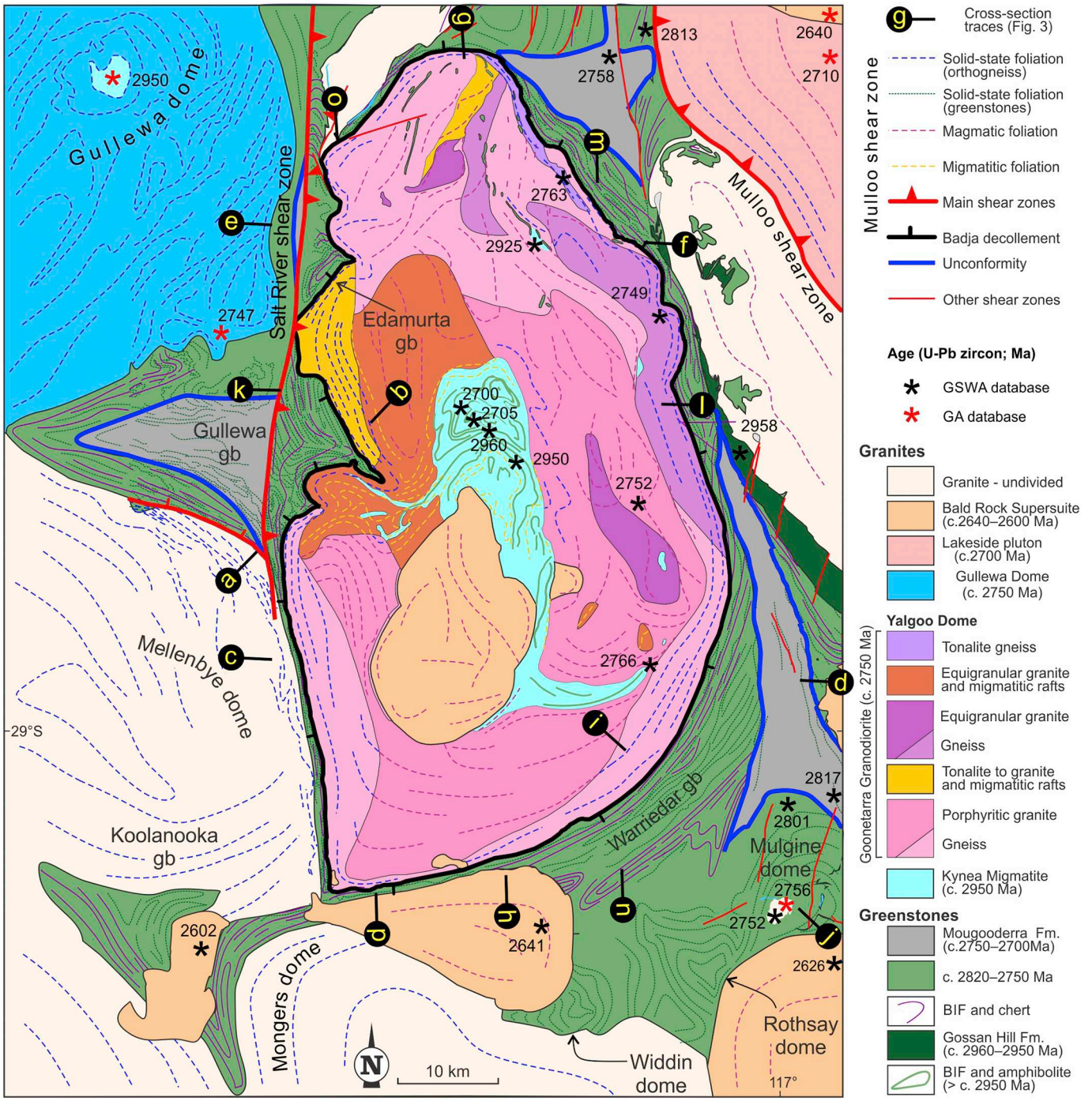

Fig. 2. Geological map of the Yalgoo area, highlighting the dome-and-keel pattern defined by the granite-greenstone boundaries. The area includes four large, deeply-eroded domes (Gullewa, Mellenbye, Mongers and Yalgoo domes) and three small domes (Mulgine, Rothsay and Widdin domes).

fabrics towards the structurally-higher greenstone cover, where greenschist-facies conditions prevail. Despite these differences, we use the same labels (S_D and L_D) for the domal SL fabric across different domains and lithologies, to highlight the composite, but geometrically and kinematically coherent nature of such fabric.

Although data presented here cover the whole Yalgoo area, our attention is mainly focused on the Yalgoo dome, because it is considerably better exposed than the adjacent domes, and shows a continuous, mappable greenstone envelope. Therefore, we first define the chief characteristics of the domal fabric in the Yalgoo dome and its greenstone cover (Section 3.1), and then those representative of the broader Yalgoo area (Sections 3.2 and 3.3).

3.1. Yalgoo dome

This section outlines the chief structural features of the granite–migmatite core of the Yalgoo dome and its greenstone cover, which also represent the envelope of the adjacent domes (Fig. 2). The Yalgoo dome shows an elliptical outline (90 by 50 km in map view), and includes an inner granite–migmatite domain and an outer orthogneiss domain.

3.1.1. Granite–migmatite dome core

The structural evolution of the Kynea Migmatite, forming the inner part of the dome, is detailed in Clos et al. (2019a), and therefore only the chief and complementary structural features of the domal fabric are

Table 1
Summary of relevant geochronological constraints (U–Pb in zircon) for the Yalgoo dome area.

	Age (Ma)	Formation	Sample ID	Easting	Northing	Reference
	Greenstone domain					
	2758 ± 4[a]	*Mudstone, Mougooderra Fm.*	*211101*	*479552*	*6868859*	Lu et al., *2016*
	2801 ± 6	metamorphosed quartz diorite	198294	500221	6780551	Lu et al., 2016a
	2813 ± 3	Metadacite, Norie Group	198298	483155	6867425	Lu et al., 2016b
	2958 ± 6	Metadacite, Gossan Hill Fm.	203701	491184	6826564	Lu et al., 2018a, 2018b
	Gullewa dome					
	2747 ± 3	Metasyenogranite	99969142	436558	6830492	Cassidy et al., 2002
	2950 ± 6	Kynea migmatite (core)	88-200	426698	6858004	Cassidy et al., 2002
	Mulgine dome					
	2752 ± 8	monzogranite gneiss	207628	497923	6771884	Wingate et al., 2018
	2756 ± 20	monzogranite gneiss	99964016C	497945	6771118	Cassidy et al., 2002
Yalgoo dome	Orthogneiss domain					
	2749 ± 4	*Goonetarra Granodiorite*	*155822*	*485369*	*6835504*	Wingate et al., *2015a*
	2763 ± 6	*Goonetarra Granodiorite*	*214101*	*475798*	*6850260*	Lu et al., *2017b*
	Granitic domain					
	2752 ± 13	*Goonetarra Granodiorite*	*155858*	*263510*	*6757191*	Lu et al., 2017a, 2017b, 2017c
	2766 ± 4	Goonetarra Granodiorite	155875	484414	6796336	Lu et al., 2020b
	2925 ± 5[b] 2757 ± 6[c]	Kynea Migmatite[d]	155843	471829	6843495	Lu et al., 2020a
	Core					
	2919 ± 12	Kynea Migmatite	83339	467438	6825531	Wiedenbeck and Watkins, 1993
	2956 ± 58	*Kynea Migmatite*	*155879*	*470656*	*6818779*	Wingate et al., 2015a, 2015b
	2960 ± 10	*Kynea Migmatite*	*209689*	*467502*	*6823605*	Lu et al., *2017b*

Fig. 2 for sample location.
Samples in italic were also analysed for zircon Lu-Hf isotopes.
Sample locations are referenced using Map Grid Australia (MGA) coordinates, Zone 50.
[a] Maximum depositional age.
[b] Age from melanosome.
[c] Age from leucosome.
[d] Layered migmatitic raft within the Goonetarra Granodiorite.

summarized here (and in Supplementary file S3). The Kynea Migmatite is a stromatic metatexite (Sawyer, 2008) interlayered with older greenstone rafts (Fig. S3.1a). S_D (S_1 in Clos et al., 2019a) is a variably-oriented, steeply-dipping gneissic foliation ((i) in Fig. S3.1b), axial planar to mesoscale sheath and isoclinal folds (Clos et al., 2019a, 2019b; Fig. 5.2 in Fenwick, 2014). It is invariably parallel to lithological boundaries, bearing a subvertical stretching and mineral lineation (L_D), coaxial with fold axes ((ii) in Fig. S3.1b). On subvertical exposures, mantled porphyroclasts, S–C and C′ subfabrics indicate core-up shear sense (Fig. S3.1c). Boudinage of the more competent greenstone

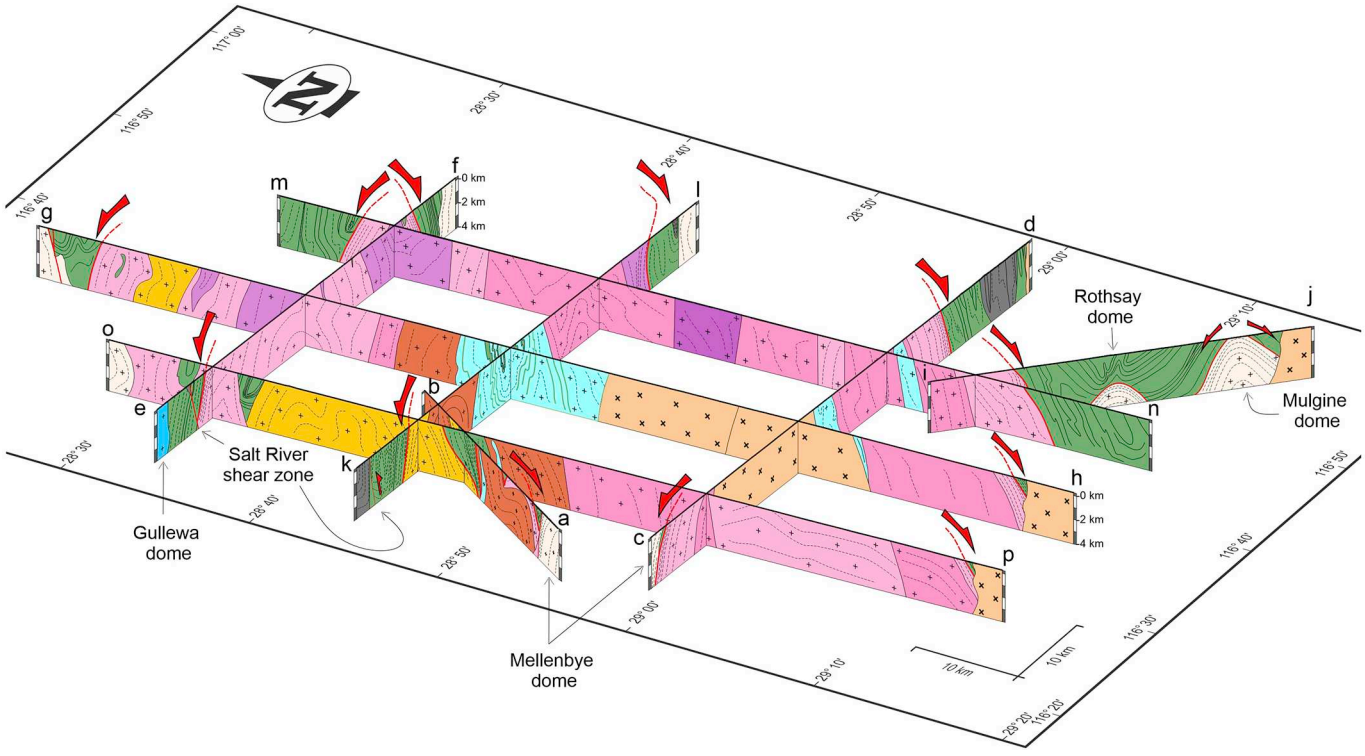

Fig. 3. Composite isometric cross section array illustrating the three-dimensional structure of the Yalgoo dome area. Legend as in Fig. 2. The location of each cross-section is indicated in Fig. 2.

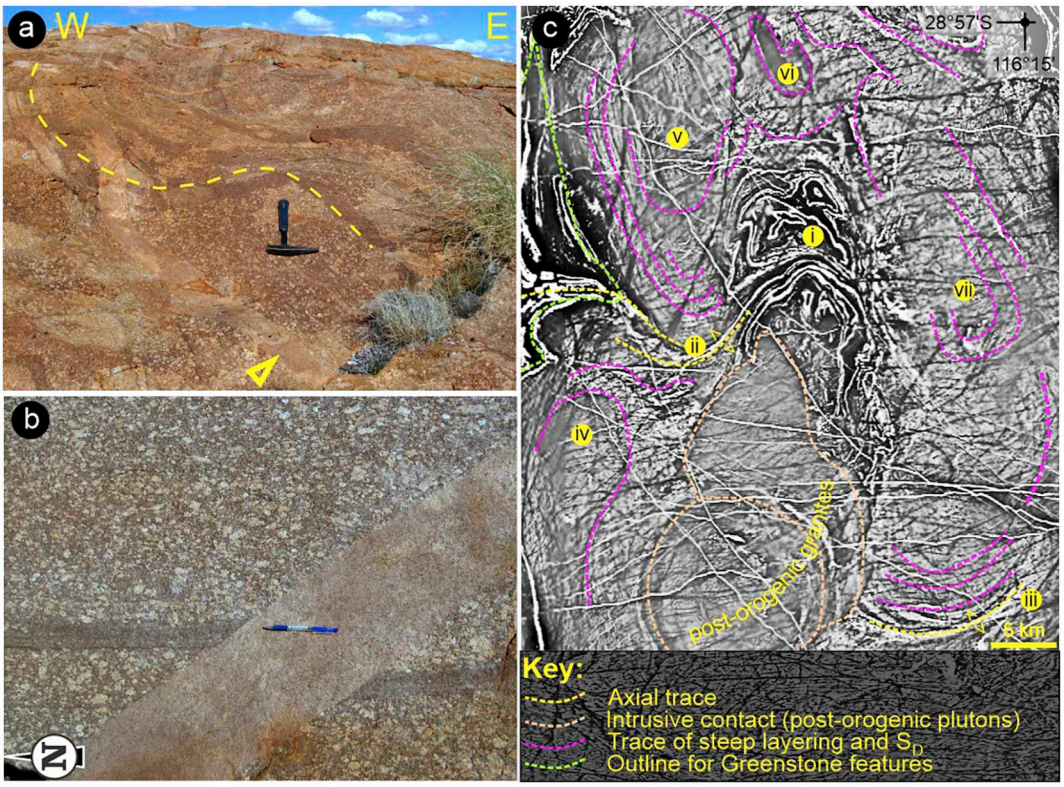

Fig. 4. Typical mesoscale magmatic and solid-state end-member fabrics in the Goonetarra Granodiorite. All field photographs are from subhorizontal exposures, unless otherwise indicated. (a) Magmatic layering in porphyritic granite, due to variable content of K-feldspar phenocrysts, defining open, synmagmatic upright folds, here truncated by aplite veins (arrowhead). (b) Detail from the same outcrop in (a), showing the magmatic foliation S_D, defined by aligned euhedral K-feldspar phenocrysts and truncated by a microgranite dyke. (c) Map showing the first vertical derivative (1VD) of Reduced-to-Pole Total Magnetic Intensity, centered on the granite–migmatite core of the Yalgoo dome. Numbers (i)–(vii) identify subareas discussed in the text. (d) Gneissic S_D in porphyritic granite exposed along the Badja décollement. Horizontal view at high-angle to the steeply plunging L_D, showing elongate quartz ribbons and biotite trails, wrapping around rounded mantled K-feldspar porphyroclasts with elongate tails and local feldspar boudinage (arrowhead). (e) Subvertical exposure of porphyritic gneiss from the same outcrop in (d). Sigma-type mantled K-feldspar porphyroclasts indicate dome-up, normal kinematics.

rafts was accompanied by in-situ partial melting of amphibolite (Fig. S3.1d), indicating that the domal fabric developed under migmatitic conditions.

The granitic domain typically retains primary magmatic fabrics (Fig. 4a and b), with S_D subparallel to the magmatic layering (Fig. 4a) and aligned migmatitic rafts, showing variable orientation and roughly concentric map-scale patterns (Fig. 2; plot (i) in Fig. S3.1b). The series of map-view concentric circular patterns defined by lithological boundaries in the Kynea Migmatite ((i) in Fig. 4c) represent horizontal sections through multiscale vertical sheath folds (see also Clos et al., 2019a). Migmatites also define tight, ~15 km-long curved antiformal ridges aligned with greenstone keels ((ii) and (iii) in Fig. 4c), separating domains in which magmatic/migmatitic layering defines map-view concentric trajectories, revealing the occurrence of at least four main subdomes within the Yalgoo dome ((iv)–(vii) in Fig. 4c).

The transition to the orthogneiss domain towards the margin of the dome occurs through the progressive development of gneissic to mylonitic fabrics (Figs. 4e, e and S5.2). Here, S_D is outward-dipping at the scale of the dome (Fig. 3), defining a first-order (map-view) concentric pattern, while L_D shows a dome-scale radial (outward-plunging) orientation (Fig. 5a). Kinematic indicators, such as S–C and C′ subfabrics and mantled feldspar porphyroclasts, invariably indicate normal kinematics (Fig. 4e) along all granite–greenstone boundaries. Within the ~4 km-thick orthogneiss domain, solid-state overprint progressively increases towards the granite–greenstone contact, which represents the zone of highest finite strain. In the case of the Yalgoo dome, such high-strain zone is nearly continuously exposed, and it is defined here as the Badja décollement.

3.1.2. *Contact with greenstone cover*

The strain distribution in the greenstone cover of the Yalgoo Dome mirrors that observed in the granite gneisses, with the highest strain occurring along the boundaries with all the granite–gneiss domes. However, finite strain and bulk structural features in the greenstone cover vary in detail, as a consequence of rheological heterogeneities due to lithological complexity. Competent lithologies such as amphibolite display a single, prominent fabric, where S_D and L_D are parallel to those in the underling granite gneiss (Fig. 5b). Independently from S_D orientation, L_D shows pitch angles $> 45^{\circ}$ in ~85% of the structural sites along the margins of the best-exposed domes (with 35% of sites showing pitch $> 80^{\circ}$, Fig. 5c). This, together with their radial distribution around the Yalgoo Dome (Fig. 5a and b), indicates bulk vertical stretching associated with doming. Conventional kinematic indicators (Fig. 6a) consistently indicate dome-up kinematics.

In contrast, three generations of superposed folds (F_{D1}–F_{D3}, with associated subfabric labelled as S_{D1}, L_{D1}, etc.) are visible in weaker,

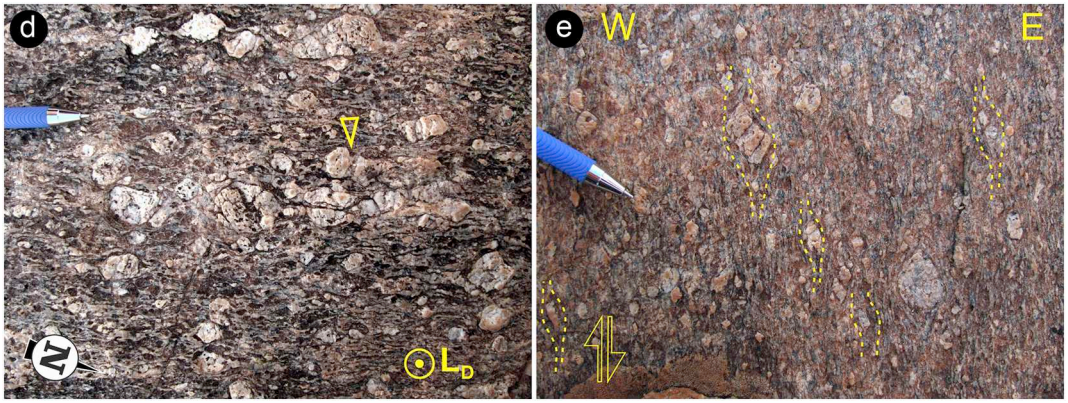

Fig. 4. (*continued*)

layered lithologies such as BIF, chert and schists. Notably, these sub-fabrics are widespread throughout the Yalgoo area, and coexist with the single SL fabric in the more competent amphibolite and orthogneiss. F_{D1} folds include isoclinal and sheath folds with steeply plunging axes (A_{D1}; Fig. 6b) coaxial with L_D, and are associated with a prominent transposition foliation (S_{D1}, Fig. 6c). Field evidence indicates that F_{D1} folds predate the development of the angular unconformity (VII in Fig. S1.2). F_{D1} are refolded by tight to isoclinal folds (F_{D2}), which are essentially coaxial and coplanar with F_{D1}, and are associated with a spaced crenulation cleavage (Fig. 6d, e). F_{D3} are coplanar with F_{D1} and F_{D2} folds but they have sub-horizontal fold axes (A_{D3}, Fig. 6f, g).

3.2. Other granite–gneiss domes

3.2.1. Deeply-eroded, large domes: Gullewa, Mellenbye and Mongers domes

The Gullewa, Mellenbye and Mongers domes are exposed along the western and southern flanks of the Yalgoo dome, between the Gullewa and the Koolanooka greenstone belts (Figs. 2 and 7a). Since the outline of these domes is only partially preserved, their exact size and shape are not fully constrainable. However, field data indicate that these domes are steep-sided, showing comparable size to the Yalgoo dome (Fig. 2). Chief characteristics of the domal fabric are identical to those described for the Yalgoo dome, and include a concentric pattern of domal S_D, in one case wrapping around a migmatite core (Gullewa dome), and concordant to dome margins (Figs. 2 and 5a). As for the Yalgoo dome, S_D in these domes exhibits a transition from magmatic to solid-state flow towards dome margins, commonly bearing a down-dip L_D (Fig. 5a–c).

3.2.2. Small-scale domes: Mulgine, Rothsay and Widdin domes

A cluster of three small domes (long axes: 5–10 km) occurs almost entirely buried below the Warriedar greenstone belt, pinched between the southern margin of the Yalgoo dome and the Mongers dome ((ix)–(xi), Figs. 2, 3 and 7b). The Mulgine dome is the only one with the granitic core exposed (Fig. 8), showing a flat-lying dome roof that coincides with a high-strain décollement, associated with core-up kinematics. S_D in the granitic core is horizontal to gently outward-dipping, carrying radial, outward-plunging L_D (Fig. 8). L_D has smaller pitch angles than the other domes (Fig. 5c), but this may represent an artefact generated by the difficulty in measuring precise orientations of the subhorizontal foliations S_D (Fig. 8). The granitic cores of the Widdin and Rothsay domes are revealed by the domal shape of their mantling greenstone cover and their inferred granitic cores are not exposed (cross section i–j in Fig. 3). Here, S_D and lithological boundaries show concentric, outward-dipping domal patterns, (Figs. 7 and 8), bearing a down-dip L_D that shows radial arrangements at the scale of each dome (Fig. 8). Notably, these three domes show a misorientation of their long axes, which are northeast-trending for the Mulgine and Widdin domes, and northwest trending for the Rothsay dome, and therefore also misoriented with the north trending long axis of the Yalgoo dome (Figs. 2 and 7b).

3.3. Greenstone keels separating domes

In this section, we focus on three greenstone sequences cropping out as broad synforms between domes, defining cuspate triangular regions where each margin is parallel and conformable with the curved dome margins. In these greenstones, structural features and superposed fabrics are comparable to those described for the greenstones in the proximity of the Yalgoo dome (Section 3.1.2). Along the western flank of the Yalgoo Dome, the Gullewa and the Koolanooka greenstone belts are synformal keels pinched at triple points between the four large adjacent domes (Figs. 2 and 7a; see also Bouhallier et al., 1995, for a similar case). The Koolanooka greenstone belt (Fig. 7a) is preserved as tight, northwest-plunging and subvertical synform (Fig. 5b), showing steeply northwest-plunging L_D parallel to the axis of mesoscale folds. Notably, both L_D and fold axes in the Koolanooka greenstone belt are subparallel to L_D in the Mongers dome. A similar concordance is observed between the mean orientations of S_D and L_D in the Gullewa greenstone belt and the surrounding Gullewa and Mellenbye domes (Fig. 5b, compare stereonets on lower left).

The Warriedar greenstone belt (Figs. 2 and 7b) exposes map-scale greenstone structures that result from the interference between the three adjacent small dome roofs described above. In the center of the belt, the Jasper Hill syncline is pinched between these three small domes and the Yalgoo dome ((xii), Fig. 7b). Here, the arcuate axial traces of the second-order folds wrap the Yalgoo dome margin in the northwest, and the Mulgine dome margin in the southeast, producing a peculiar fan-shaped geometry for the overall Jasper Hill syncline. Closer to the Badja décollement, BIF layers define tight, steep isoclinal folds with curved axial traces wrapping the Badja décollement ((xiii), Fig. 7b). Notably, these map-scale F_{D1} folds are truncated by the infra-greenstone unconformity at the base of the Mougooderra Formation ((xiv), Fig. 7b), consistently with outcrop-scale observations ((vii) in Fig. S1.2a).

3.4. Shape of the finite strain ellipsoid

This section provides qualitative estimation of the shape of the finite-strain ellipsoid (FSE) throughout the Yalgoo area. Both the core of

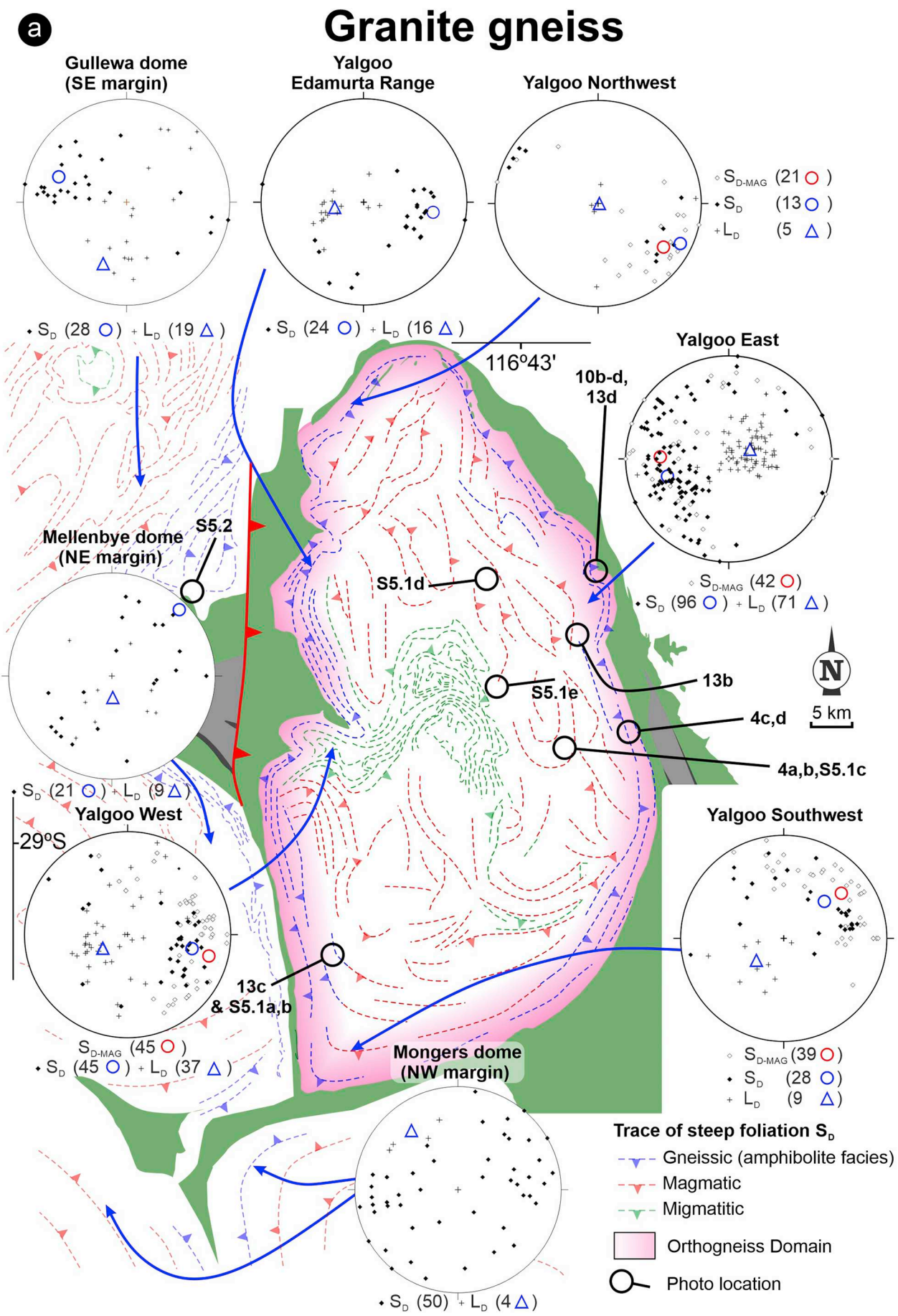

(caption on next page)

Fig. 5. (a) Simplified map of the granitic domes of the Yalgoo area, with equal-angle projection plots (lower hemisphere) for each exposed domain. In each dome, S_D is broadly concentric and conformable to dome margins, showing a transitional character from magmatic to gneissic (subsolidus). (b) Same as (a) but focused on the greenstone belts. Equal-angle projection plots (lower hemisphere) for each structural domain identified within the greenstone cover. For plots in (a) and (b), number of measurements and symbols for mean values are reported in brackets. Symbols as for (a), except as indicated. (c) Pitch of L_D vs. azimuth of S_D for the greenstone sequence, for the Yalgoo and Mulgine domes, for the northeastern portion of the Mellenbye dome, and the southeastern portion of the Gullewa dome. Note that in general lineation is down-dip and radial. For the greenstone sequence, Yalgoo and Mulgine Domes, where data are available for the entire dome, L_D covers the entire 360° spectrum, generally plunging steeply down-dip.

the Yalgoo dome and ~80% of the exposed high-strain zones along the granite–greenstone boundaries in all domes consistently show a sub-horizontal extension component perpendicular to L_D (Figs. 4d and S3.1d), indicating bulk flattening associated with vertical stretching. The Yalgoo dome exhibits several small greenstone keels protruding towards the granite–migmatite dome core (Figs. 2 and 7); six of them are partially exposed (Fig. 9a), and only the Gnows Nest keel offers continuous exposure (Fig. 9b). Here, S_D dips towards the centre of the keel, carrying a steeply-plunging L_D (Fig. 9b and c). Steep F_{D1} isoclinal to sheath folds in greenstones show curved axial traces, wrapping the trace of the Badja décollement. Notably, S and Z symmetry of F_{D1} folds shows a systematic spatial distribution (Fig. 9b and c), reflecting flow of supracrustal material towards the keel (Brun et al., 1981). S_D is overprinted by a subvertical, local, spaced crenulation cleavage (S_{D4}) that is axial planar to the greenstone keel and to subvertical folds (Figs. 9b, c and 10a). Orthogneisses flanking greenstone keels display L > S to L tectonite (Fig. 10b–d), grading to SL tectonite at distances > ~1 km from keel regions. In contrast, in greenstones L tectonites are restricted to the hinge area of plurimetric F_{D1} folds (Fig. 10e), grading to SL tectonites towards fold limbs. Here, the transition between end-member tectonite types occurs quite abruptly at the meter scale, similarly to what is described in Sullivan (2013). Notably, both constrictional fabric and S_{D4} are exclusively spatially associated with greenstone keels (Figs. 9 and 10). Along the western flank of the Yalgoo dome, L > S to L tectonites occur in chert conglomerate pinched between the Yalgoo and the Mellenbye domes (Brandy Hill, Figs. 7b and 9a), reflecting a local constrictional regime within a high-strain triple point between the two adjacent domes (Bouhallier et al., 1995; Collins et al., 1998).

4. Orogenic fabric

The domal fabric described above is overprinted by a weakly- to moderately-pervasive, north-striking and steeply east dipping orogenic fabric that is heterogeneously developed throughout the study area (Fig. 11a). It traverses the region without any systematic geometrical relationships with the dome-and-keel regional architecture. It is subparallel to the large-scale, north-striking structural grain that typifies the Youanmi Terrane (Fig. 1), and subparallel to the Mulloo shear zone (Figs. 2, 11a), a large-scale structure that was active during the emplacement of the c. 2700 Ma Lakeside pluton (Zibra, 2012; Zibra et al., 2014). The steeply east-dipping Mulloo shear zone has down-dip stretching lineation (Fig. 11a), and it was active during magma emplacement and during subsequent syndeformational cooling. It is characterized by top-to-west kinematics, marked by a prominent magmatic foliation and layering, and shearing of migmatitic rafts (Fig. 11b), and gave rise to mylonitic fabrics developed along the base of the shear zone (Figs. 11c and S4.4a). Since the main focus of this study is on the domal fabric, only the chief features of the orogenic fabric are outlined here (and in the Supplementary file S4).

The orogenic foliation (S_{OR}) in the study area is mainly visible along the Salt River shear zone (Fig. 12a). This structure shows north-striking, steeply dipping mylonitic foliation associated with steeply plunging stretching lineation and reverse kinematics (Fig. S4.1a–c). In this area, the Badja décollement is locally reworked as reverse, retrograde shear zone showing top-to-southeast kinematics (Fig. 12a–c). In felsic gneisses, biotite is replaced by syntectonic chlorite (Fig. 12b), suggesting retrograde metamorphic conditions. In supracrustal lithologies, S_{OR} appears as spaced crenulation cleavage and is axial planar to meter-scale, disharmonic parallel and kink folds with steeply plunging axes (Fig. S4.1d–f). Two sets of north-striking structures overprint the domal fabric in the deeper crustal level exposed in the core of the Yalgoo dome (Fig. S4.2), reflecting periods of bulk east–west shortening (D_2 and D_3 in Clos et al., 2019a). The earlier one developed under migmatitic conditions (Fig. S4.3), while younger reverse shear zones are confined within c. 2700 Ma north-striking granite dykes (Clos et al., 2019a). These local structures are therefore grouped here under the orogenic fabric.

5. Microstructures

In order to integrate outcrop- to map-scale observations, we outline here (and in the Supplementary file S5) chief microstructural features of the domal fabric. Felsic gneisses from the Kynea Migmatite and the surrounding, younger granites show comparable microstructures (Fig. 13a–c). K-feldspar and plagioclase porphyroclasts are mantled by coarse-grained polygonal aggregates of the same phases (up to 500 μm in size, Fig. S5.1a), reflecting feldspar recrystallization at high temperature (Rosenberg and Stünitz, 2003). Quartz forms elongate, mono- to polycrystalline, coarse-grained ribbons. Individual quartz grains show chessboard subgrain boundary pattern (Fig. S5.1b, c), indicating deformation in the high-quartz field, at near-solidus temperatures (Kruhl, 1996). Quartz grain boundaries are deeply sutured, suggesting widespread recrystallization through grain boundary migration (Stipp et al., 2002). K-feldspar occurs as narrow films coating quartz and plagioclase grain boundaries (Fig. 13a), or filling microfractures (Fig. 13b and c), reflecting syntectonic migration of former residual melt towards low-pressure sites (Sawyer, 1999). Plagioclase–quartz grain boundaries are commonly cuspate and lobate (Fig. 13a and c), indicating deformation at upper amphibolite facies conditions (Gower and Simpson, 1992). Pegmatite gneiss contains the garnet-sillimanite assemblage (Fig. S5.1d), indicating upper-amphibolite facies conditions. S_D in amphibolite rafts is a continuous foliation defined by hornblende–plagioclase ± clinopyroxene ± quartz, while tonalitic leucosomes include peritectic clinopyroxene (Fig. S5.1e). As a whole, these microstructures from the inner portions of the Yalgoo dome reflect deformation at near-solidus temperatures, in agreement with field observations and metamorphic data (Clos et al., 2019a, 2019b).

S_D in felsic gneisses exposed along the Badja décollement and the other granite–greenstone boundaries includes elongate and coarse-grained quartz ribbons, together with trails of recrystallized feldspar, biotite and epidote, wrapping around plagioclase and K-feldspar porphyroclasts (Fig. 13d). Both plagioclase and K-feldspar show evidence of widespread recrystallization. Aggregates of recrystallized, polygonal grains are 100–200 μm in size (yellow arrowhead, Fig. 13d) and, near

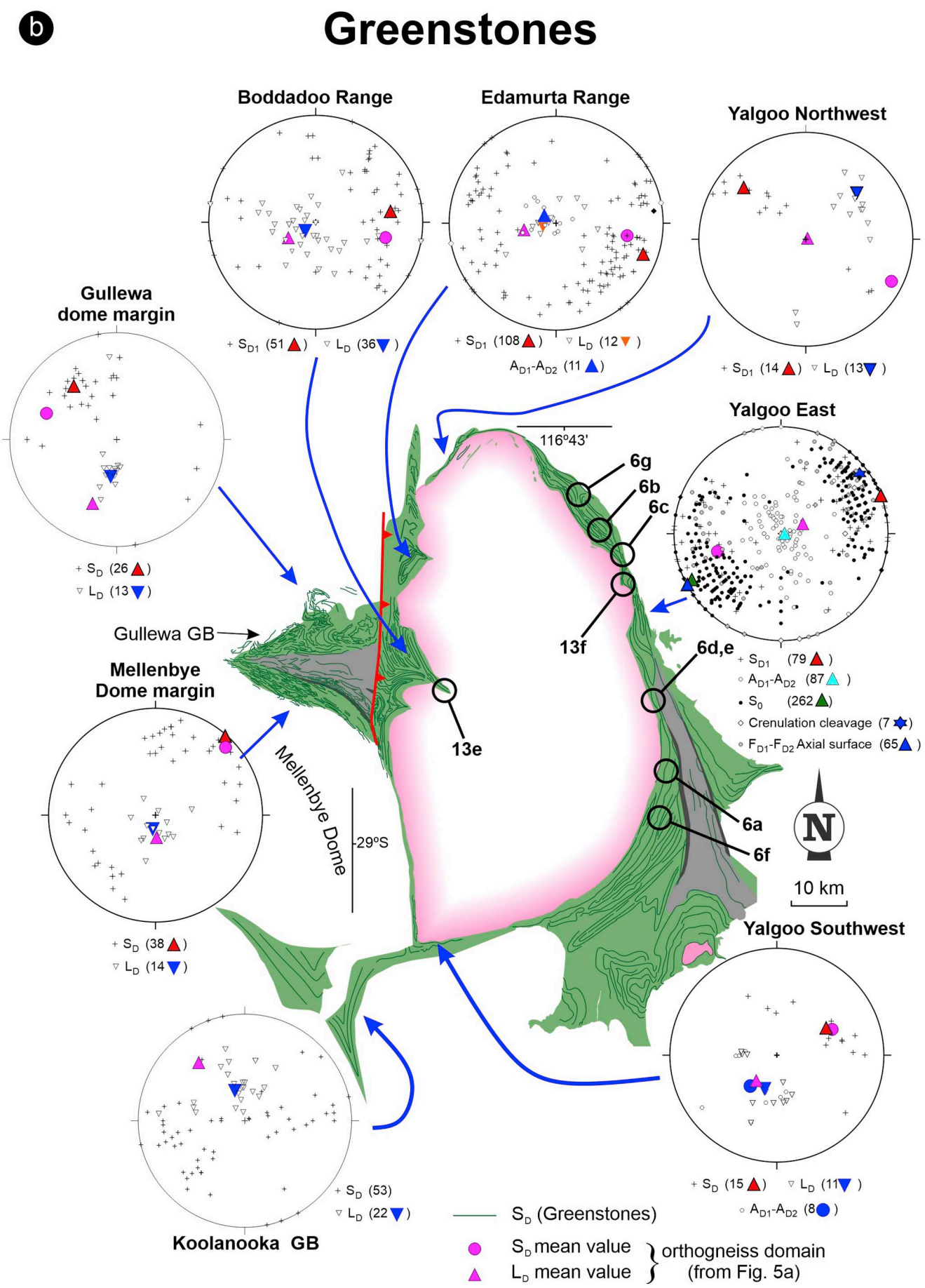

Fig. 5. (*continued*)

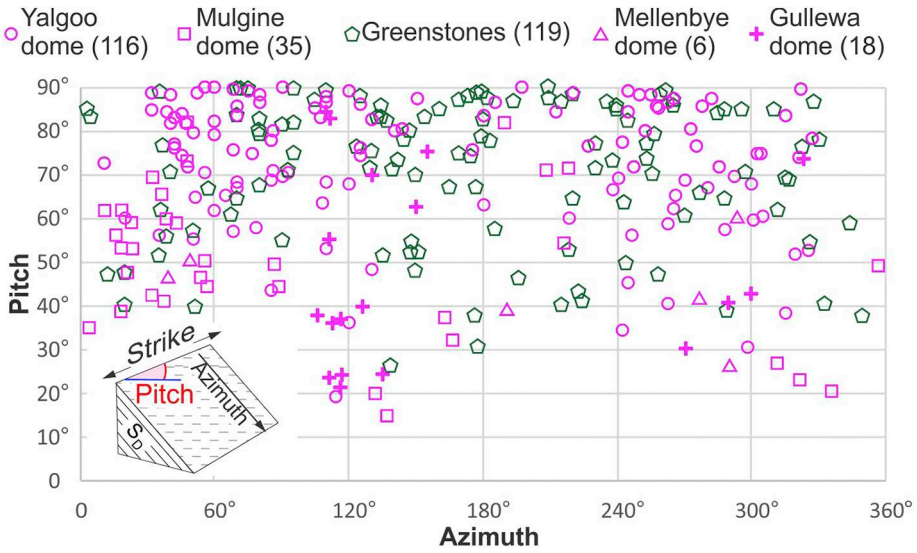

Fig. 5. (*continued*)

the margins of porphyroclasts, they grade into subgrains of comparable size, suggesting that feldspar recrystallization resulted from dominant subgrain rotation (Rosenberg and Stünitz, 2003). Strain-induced myrmekites in K-feldspar porphyroclasts (white arrowhead, Fig. 13d) indicate shearing at amphibolite-facies conditions (Simpson and Wintsch, 1989). Microfracturing in feldspar porphyroclasts is uncommon, suggesting that the shearing temperature along the main décollements did not fall significantly below 500 °C (Passchier and Trouw, 2005). This is also supported by the coarsely-lobate quartz-quartz grain boundaries (Fig. 13d), which suggest quartz recrystallization via grain-boundary migration at temperature ≥ ~500 °C (Stipp et al., 2002). In the hanging wall of the main décollements, granoblastic mafic gneisses contains the hornblende–plagioclase ± epidote assemblage, while late-tectonic garnet porphyroblasts locally occur in amphibolite within greenstone keels (Fig. 13e). Microscale folds in BIF typically show a continuous axial-planar foliation marked by aligned quartz, magnetite and amphibole (S_{D2}; arrowhead in Fig. 13f), suggesting amphibolite facies conditions (Klein, 2005).

5.1. Domal fabric: quartz c-axis crystallographic preferred orientation

In order to constrain the deformation temperature, type of strain and bulk flow, and prevailing shear sense throughout the study area, we determined the quartz crystallographic preferred orientation (CPO) in 28 samples from the Yalgoo dome, and one sample for the Mulgine and Gullewa domes (Fig. 14; Fig. S6.1 for sample locations). Samples were collected from outcrops showing the domal fabric only, except sample 155827, which is representative of S_{OR} developed within a c. 2700 Ma north-striking granite dyke (core of Yalgoo dome). Thin sections were prepared normal to S_D and parallel to L_D. For the Yalgoo dome, results are presented as an ideal cross section from the migmatitic core towards the greenstone cover (Fig. 14). All samples were scanned with an automated fabric analyser microscope (Peternell et al., 2010; Wilson et al., 2007), and the quartz c-axis CPO was determined using the FAME (Fabric Analyser Microstructure Evaluation) software (Hammes and Peternell, 2016).

Although the CPO is generally moderately-developed, clear maxima can be identified in most samples. Four samples from the Kynea Migmatite (155879, 155880, 155884 and 209689) show maxima at low-angle from L_D, which is indicative of dominant prism ⟨c⟩-slip and reflect shearing at near-solidus temperatures (Mainprice et al., 1986; Stipp et al., 2002). Secondary maxima at low-angle from the Z axis (in 155880 and 155884) indicate the subordinate activity of basal ⟨a⟩ slip. Likewise, the near-X maximum shown by sample 155827 indicates that reverse shearing along c 2700 Ma granite dykes (Clos et al., 2019a) occurred at near-solidus temperatures, likely during dyke emplacement.

The four samples from the granitic domain show fabrics comparable to those of the Kynea Migmatite, reflecting dominant prism ⟨c⟩-slip (possibly with a contribution of oriented grain growth in the prism ⟨c⟩ direction; Zibra et al., 2012), even though maxima here are generally weaker. 75–105° opening angles (across the Z-axis), available from four samples, point to deformation temperatures of ~600–800 °C (estimation based on Fig. 2 in Law, 2014). A similar, although more diffuse pattern associated with a near-X maximum is shown by samples 155876 and 210292 from the Mulgine and Gullewa domes.

The 16 samples from the orthogneiss domain can be grouped into three fabric types. Four samples collected in the inner, low- to moderate-strain portions of the Badja décollement shows moderately to well-developed near-X maxima. This CPO fabric is consistent with the observed microstructure, indicating that, in this portion of the Badja décollement, the gneissic S_D developed at near-solidus temperatures, and mostly under melt-present conditions (Fig. 13b and c).

Two of the 12 samples collected within the ~2 km-thick high-strain portion of the Badja décollement exhibit a well-defined near-Y maximum, which typically indicates dominant prism ⟨a⟩ slip at amphibolite-facies conditions (Passchier and Trouw, 2005). The remaining 10 samples mostly show well-defined to diffuse near-Z maxima, and subordinate maxima in near-Y and intermediate positions (e.g. samples 155806, 155839, 212730 and 210276, Fig. 14), developing a crossed girdle fabric (Lister, 1977). This indicates basal ⟨a⟩ slip, in cooperation with prism and rhomb ⟨a⟩ slip, produced the fabric observed along the Yalgoo dome margins. An incipient to well-developed crossed girdle fabric also typifies the three greenstone samples collected in the hanging wall of the Badja décollement (Fig. 14). Overall, 21 of 29 samples from the domal fabric exhibit an external fabric symmetry indicative of dominant non-coaxial flow associated with (i) upward

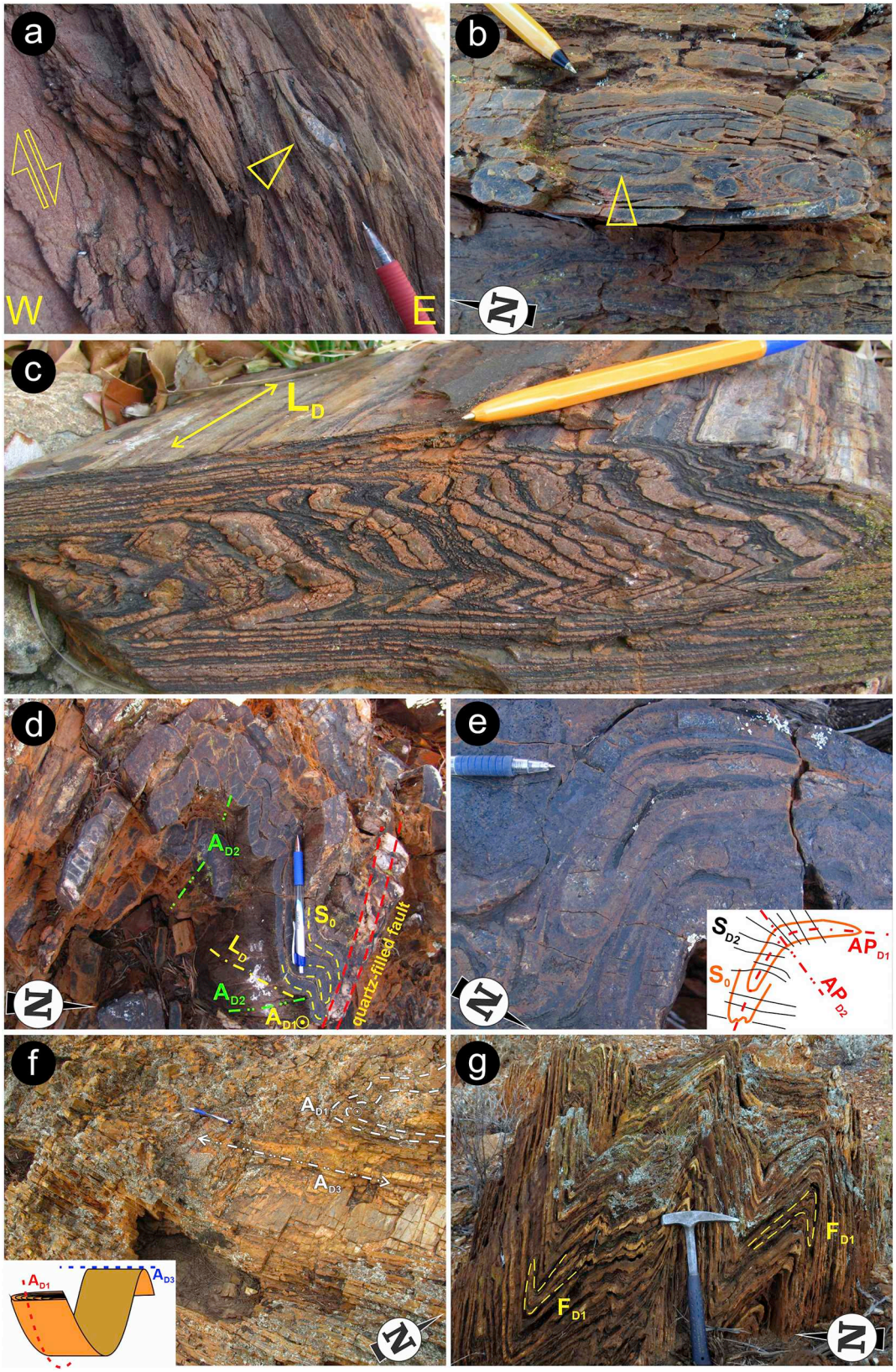

Fig. 6. Chief structures in the greenstone cover, Yalgoo area. (a) Sheared pebbly sandstone exposed a few meters above the Badja décollement, eastern flank of the Yalgoo dome. Sigmoidal chert clasts indicate dome-up kinematics. (b) Small-scale F_{D1} isoclinal and sheath (arrowhead) folds in BIF. (c) Fold hinge preserving bedding, which is otherwise transposed into S_{D1}, in highly-deformed BIF, sampled a few hundred meters above the Badja décollement (sample not in place). (d) F_{D2} folds in BIF, superposed on nearly coplanar and coaxial F_{D1}. Type 3 fold interference pattern (Ramsay, 1967). (e) F_{D1} sheath fold refolded by F_{D2} fold in BIF, with axial planar spaced cleavage (S_{D2}). (f) Steeply east-dipping exposure showing F_{D3} fold with subhorizontal axes in chert, refolding F_{D1} isoclinal folds. The inset at lower left illustrates the geometry of the superposed folds. (g) Subvertical exposure showing upright F_{D3} folds in chert, refolding isoclinal folds (F_{D1}, highlighted by yellow dashed lines). (For interpretation of the references to colour in this figure legend, the reader is referred to the web version of this article.)

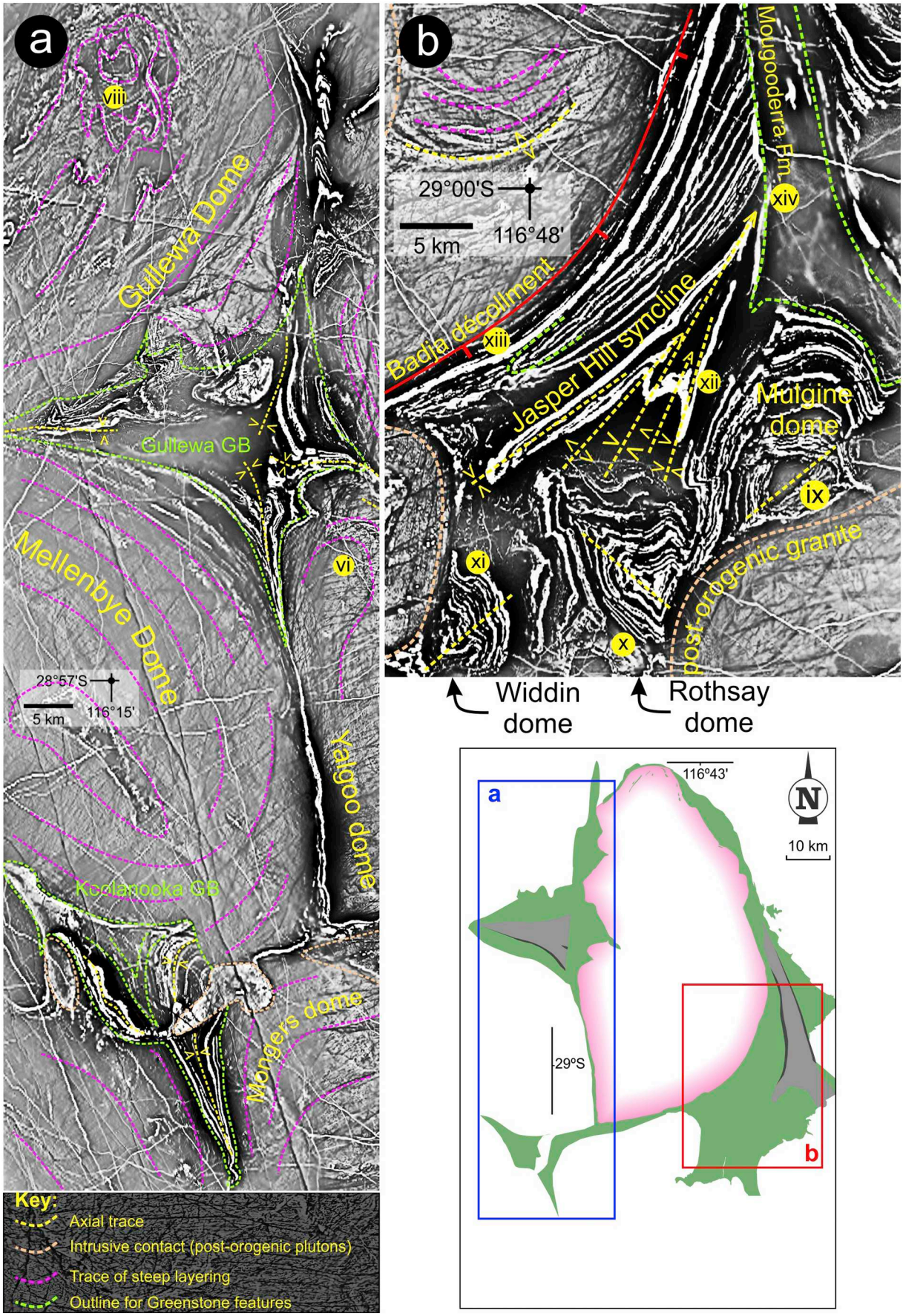

Fig. 7. Images showing the first vertical derivative (1VD) of Reduced-to-Pole Total Magnetic Intensity. Numbers (viii)–(xiv) identify subareas discussed in the text. (a) Image centered on the Gullewa and Koolanooka synformal keels, at the triple points between four adjacent domes. (b) Image centered on the Warriedar greenstone belt, covering the area between the southeast margin of the Yalgoo dome and the Mulgine (viii), Rothsay (ix) and Widdin (x) domes.

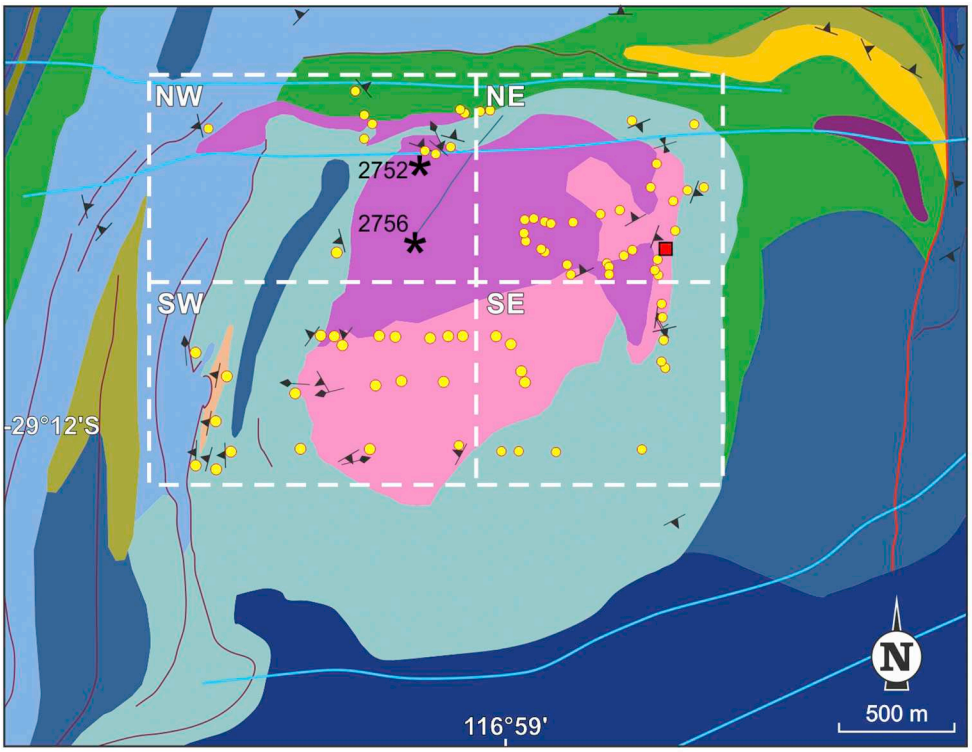

Dolerite (Proterozoic)

Granites

- Ms-bearing granite gneiss
- Tonalite gneiss

(Mulgine Dome)

Greenstones

- Metasediments
- Rhyolite
- Ultramafic schist
- Metabasalt
- Gabbro
- Dolerite
- Metaperidotite
- Amphibolite

- Banded Iron Formation
- Shear zone
- Foliation, inclined
- Foliation, dip indeterminate
- Mineral lineation, inclined
- Igneous contact, inclined
- Structural sites
- Geochronology sites
- Sample 155876 (quartz CPO)

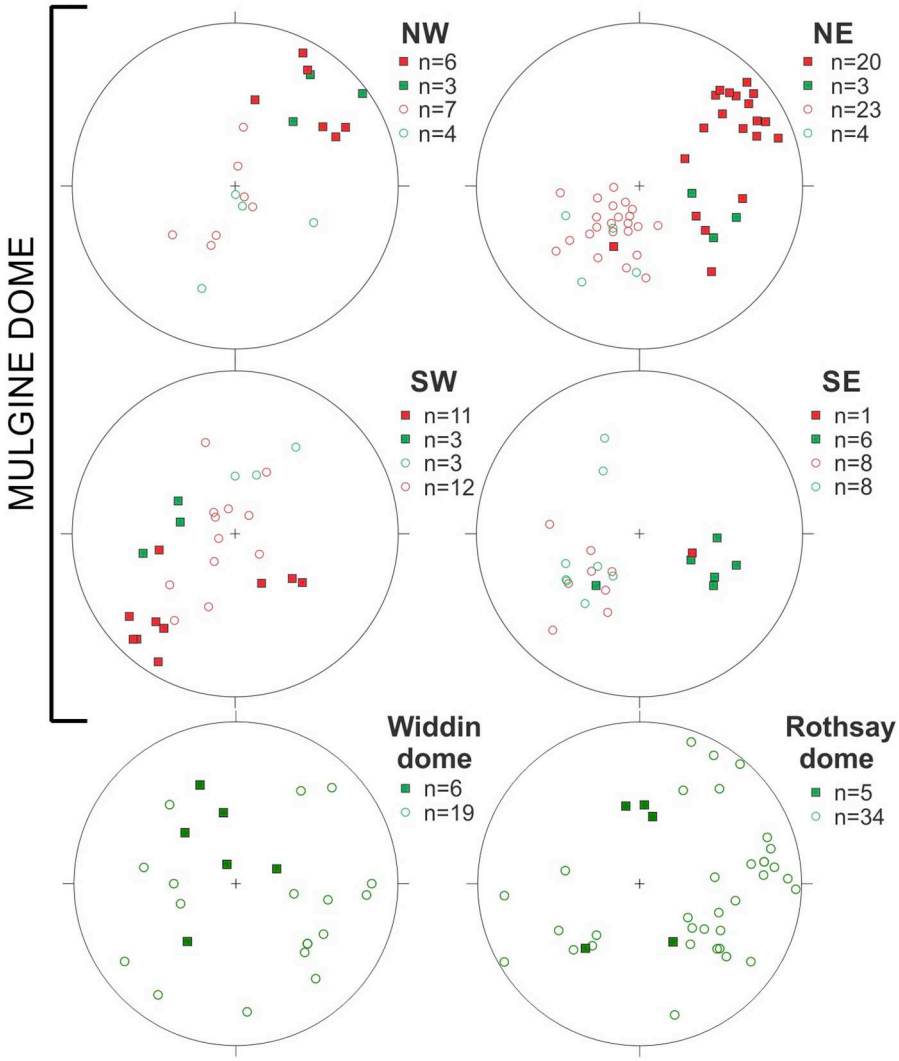

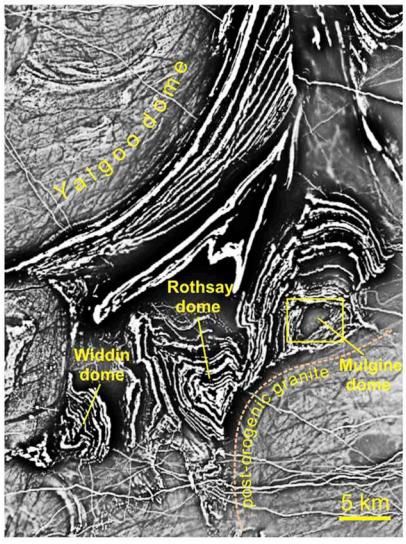

Lineation (L_D)

- Granite gneiss
- Greenstones

Foliation (S_D)

- Granite gneiss
- Greenstones

(caption on next page)

Fig. 8. Geological map of the Mulgine dome. The equal-angle projection plots (lower hemisphere) show the distribution of S_D and L_D in the four subdomains (defined by dashed boxes in the map) identified within the Mulgine dome, and in the Rothsay and Widdin domes.

displacement of the migmatitic core with respect to the surrounding granites (Fig. S3.1c), and (ii) dome-up kinematics, with respect to the greenstone cover.

6. Zircon Lu–Hf isotopes

Detrital zircons grains previously dated from a mudstone of the Mougooderra Formation (sample 211101; Table 1) comprises mostly c. 2960–2750 Ma ages, in the range of those of the granitic rocks in the Yalgoo Dome (Lu et al., 2016). The combined use of U–Pb and Lu–Hf isotopic systems to detrital zircon grains provides information about the source of sedimentary material (Zeh et al., 2008, and references therein), and so the mudstone sample 211101 is appropriate to get a broader view of the Hf values of the granitic samples eroded to form these sediments. For comparison, we selected five dated samples for zircon Lu–Hf isotope analyses (Table 1, Table S2 and Fig. 15) in order to trace sediment source, and to test whether the Mougooderra Formation was fed by granitic and migmatitic rocks of the Yalgoo dome. Analytical details are reported in Supplementary file S2. Samples 155879 and 209689 are representative of the Kynea Migmatite; samples 155822, 155858 and 214101 are representative of the Goonetarra Granodiorite.

Zircon Lu–Hf data for the c. 2960 Ma Kynea Migmatite indicates two stage depleted mantle model ages (T_{DM2}) of 3.51–3.20 Ga (median = 3.37 Ga), possibly with minor juvenile addition at c. 2.96 Ga (Fig. 15 and Table S2). This suggests Kynea Migmatite was mainly derived from reworking of Paleoarchean crust. Similarly, the c. 2763–2749 Ma Goonetarra Granodiorite yields T_{DM2} of 3.58–3.28 Ga (median = 3.45 Ga), indicating derivation from reworking of existing Paleoarchean crust or from the Kynea Migmatite.

The ages of detrital zircons in Mougooderra Formation sample 211101 suggest a maximum depositional age of c. 2758 Ma (Lu et al., 2016). The detrital zircons have similar ages (2953–2746 Ma) and T_{DM2} (3.56–2.96 Ga) to those of the Kynea Migmatite and Goonetarra Granodiorite with a further suggestion of a minor older component with T_{DM2} up to 3.88 Ga (Fig. 15).

7. Discussion

The Yalgoo area has been the focus of regional mapping and recent, small-scale structural and metamorphic studies, which provided substantial data indicative of diapirism of its migmatitic core (Clos et al., 2019a, 2019b). However, the broader three-dimensional architecture of the dome and keels described here have remained so far poorly known, and the understanding of such architecture represent the main goal of this contribution. This early architecture is significant because it predates the large-scale Neoarchean Yilgarn Orogeny, which dominates the evolution of terranes elsewhere in the craton. It is worth emphasizing here that, although the majority of our data derive from the well-exposed Yalgoo dome, and from the supracrustal greenstone envelope shared by all seven domes identified in the area, the sparsely distributed data obtained from the poorly-exposed domes are entirely consistent with the picture provided by the Yalgoo dome.

The sequence of events examined here started at c. 2960 Ma (Fig. 16a), with the emplacement of the protolith of the Kynea Migmatite into older greenstones, now preserved in the core of the Yalgoo dome as BIF/amphibolite rafts (Fig. S3.1a). The clear TTG affinity of the Kynea Migmatite (Nebel et al., 2018), together with our new zircon Lu–Hf isotope data (Fig. 15), indicate that this intrusion derived from melting of a 3.51–3.20 Ga lower crustal garnet-amphibolite source (Johnson et al., 2017; Smithies, 2000), which was part of the Paleoarchean basement of the 2960–2750 Ma greenstone succession (Ivanic et al., 2012). Greenstone development continued intermittently for the subsequent 200 Myr (Fig. 16b), producing a regional-scale, ≥8 km-thick, mafic–ultramafic supracrustal sequence (Van Kranendonk et al., 2013). However, the bulk of the structures in the Yalgoo area is Neoarchean in age, being developed in granite plutons that are c. 2760 Ma or younger.

7.1. The Yalgoo area: a case for diapirism

One of the chief features of the Yalgoo area is the regional occurrence of a single, prominent planar fabric (the domal foliation S_D) that is systematically parallel to the contacts between granite domes and greenstone belts, typically showing an increase in finite strain towards such first-order boundaries. S_D trajectory defines map-scale dome-and-basin structures, in which domal antiforms expose granite/migmatite rocks, and basinal synforms preserve portions of the supracrustal envelope (Figs. 2, 3 and 7), in a region that shows neither field nor geophysical evidence of the large-scale, east–west compression-related shear zones that typify the rest of the craton (Figs. 1 and 2). Following these observations, chief structural features of the Yalgoo area are here tested in the light of conceptual and field-based models for diapirism (Fig. 16c).

7.1.1. Type of flow in the granite–migmatite domes

One of the key observations is that the bulk of the structures in the granite–migmatite domes reflect hypersolidus flow. This is demonstrated by the widespread preservation of meso- and microstructural evidence of melt-present deformation, together with quartz CPO fabrics indicative of near-solidus temperatures, in both metatexites and surrounding granites, (Figs. 4a and b, 13a–c, 14 and S3.1b). The syn-anatexis isothermal decompression recorded by the Kynea Migmatite (Clos et al., 2019b) is entirely consistent with igneous diapirism (Teyssier and Whitney, 2002). Furthermore, the occurrence of subdomes flanked by steep migmatite ridges (Fig. 4c) is probably an expression of the internal dynamics of the rising magma bodies (Kruckenberg et al., 2018; Vanderhaeghe, 2004; Weinberg and Schmeling, 1992), which likely developed as a sequence of smaller diapirs during multiple magmatic pulses, in agreement with the ~20 Myr duration of granitic magmatism within the area (Fig. 2 and Table 1).

Pervasive subsolidus fabrics occurs only along the outer carapace of the domes (Figs. 4d, e, and 13d). Notably here quartz CPO data across the Yalgoo dome margins highlight a fabric transition from near-solidus temperature fabrics in the inner portions of the orthogneiss domain, to retrograde fabrics dominated by ⟨a⟩ slip near the granite–greenstone boundaries (Fig. 14). This indicates that the onset of shearing along the dome margins occurred during granite emplacement, while retrograde fabrics reflect syndeformational cooling of the outermost portions of the domes against the cold supracrustal country rocks, driven by the strong rheological and temperature gradients established along dome margins (Cruden, 1990).

7.1.2. Geometry and kinematics

Another fundamental observation is that all linear structures (fold axes and L_D) associated with the domal S_D show dome-scale radial

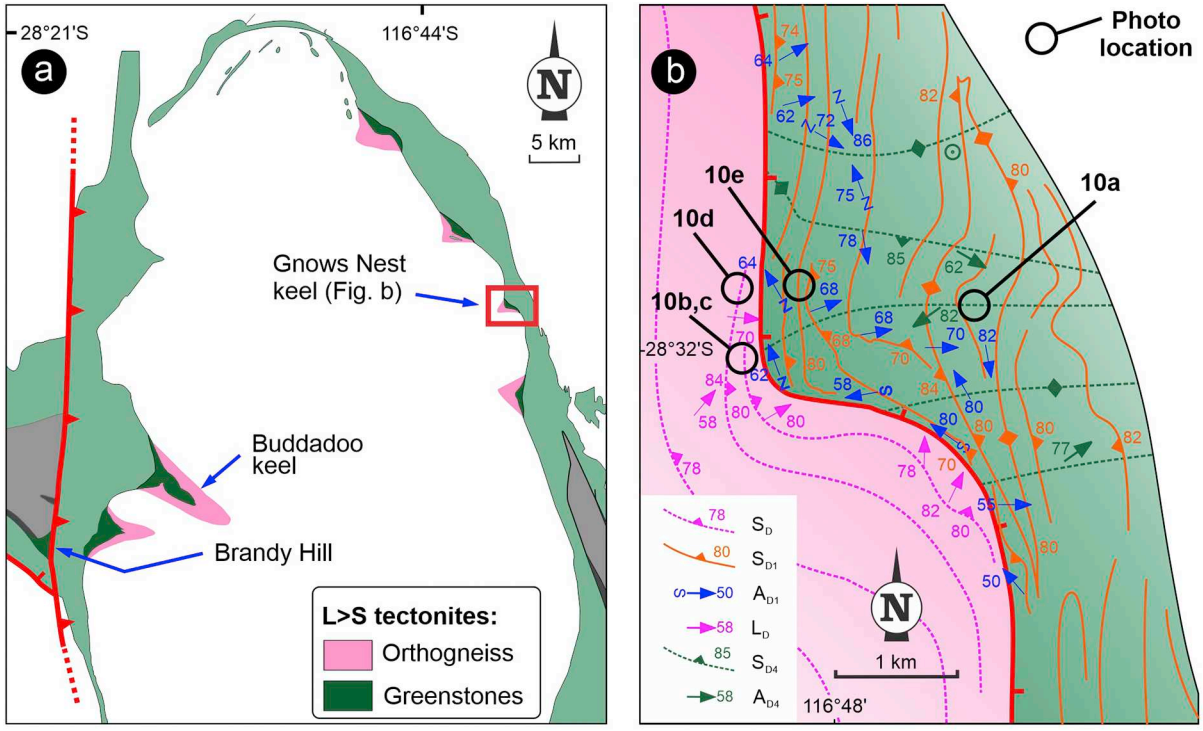

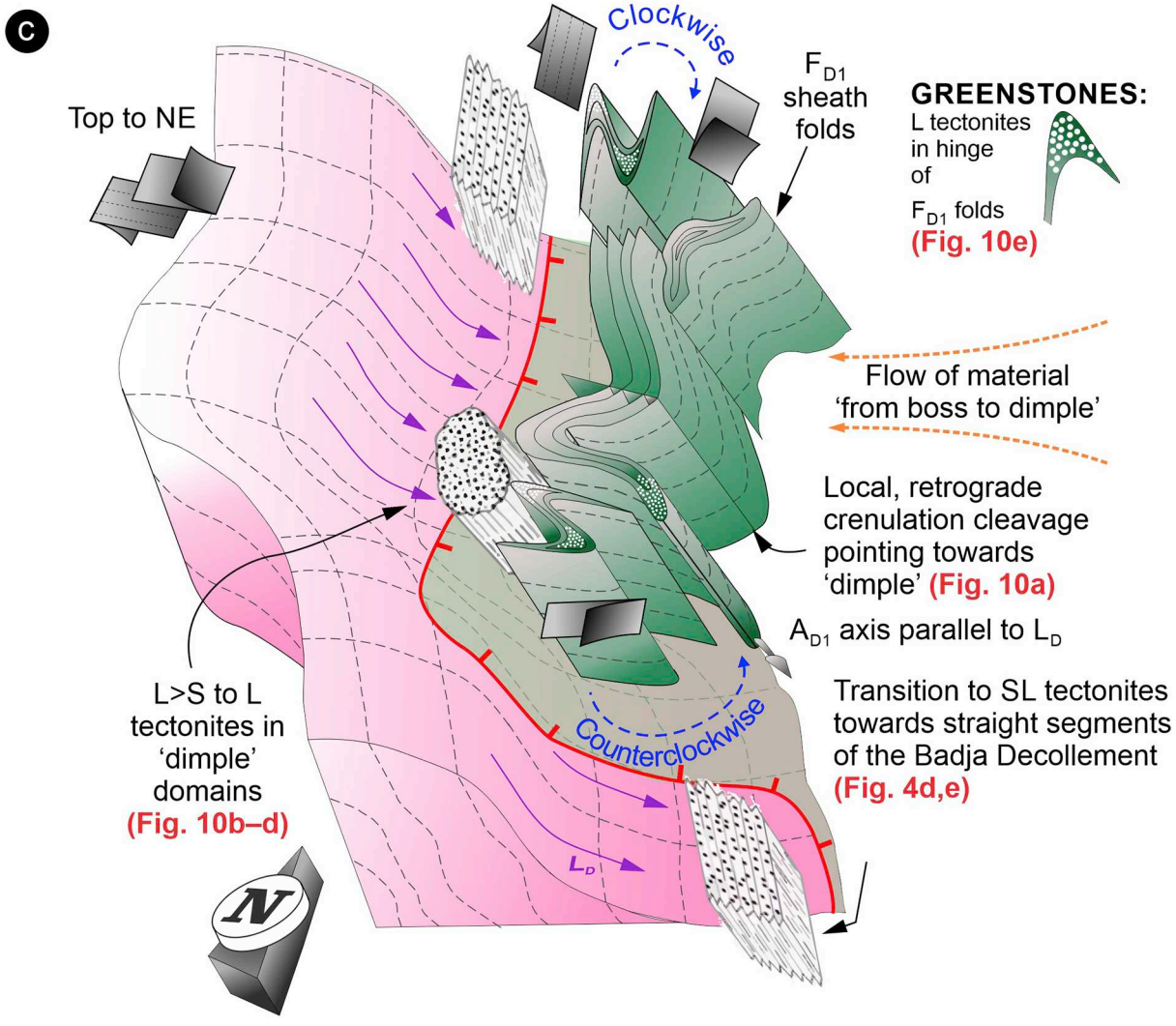

(caption on next page)

Fig. 9. (a) Simplified geological map of the northern portion of the Yalgoo dome, showing distribution of L > S to L tectonites in both the orthogneiss and overlying greenstones. The rest of the Badja décollement is characterized by S > L tectonites (Fig. 4d and e). (b) Geological map of the Gnows Nest keel, showing the main structural elements. (c) Three-dimensional sketch summarizing the first-order geometry, kinematics and structures associated with the Gnows Nest keel, showing the spatial distribution of the various types of tectonites and asymmetric folds with respect to the greenstone keel.

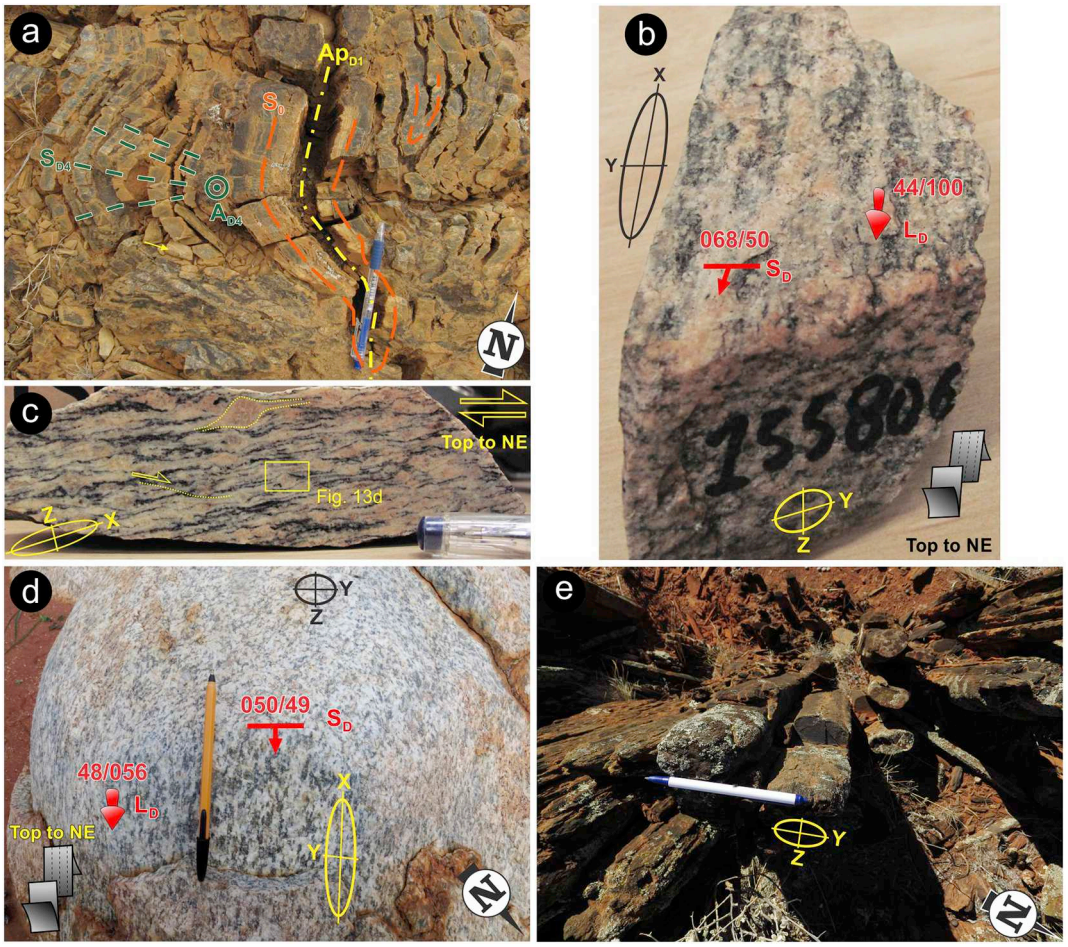

Fig. 10. Chief outcrop-scale features of the Gnows Nest keel. (a) F_{D1} isoclinal folds refolded by F_{D4} folds, showing spaced S_{D4} cleavage and prominent subvertical intersection lineation. (b)–(d) L > S to L tectonites in orthogneiss. (b) Oriented hand sample from porphyritic gneiss, with the prominent L_D visible on the foliation-parallel surface. (c) Same hand sample as in (b), here cut parallel to L_D. Sigma-type mantled K-feldspar porphyroclasts and C′ shear bands define the top-to-northeast (dome-up) kinematics. (d) Rounded boulder offering a three-dimensional view of L tectonite in tonalite gneiss. The flat, top surface shows a weakly developed S_D. In contrast, the steep sides expose the prominent L_D highlighted plagioclase, quartz and biotite recrystallized aggregates. (e) L tectonite with steeply-plunging L_D in amphibolite, seen from above, at the hinge area of a plurimetric F_{D1} fold.

arrangements in all the domes in the region (Figs. 3, 5a, b and 8), reflecting dome-up sense of shear (Figs. 3, 4e, 6a, 10c, 13d, 14 and S3.1c,). Moreover, the occurrence of vertical sheath folds in both the Yalgoo dome core (Clos et al., 2019a) and in the greenstone envelope throughout the study area (Fig. 6b and e) indicates regional-scale, bulk vertical stretching. Sheath folds in the cover sequence may represent cascading folds (Whitney et al., 2004) whose axis were progressively stretched and rotated into parallelism with the steep flow vector, while the younger subset of folds (F_{D3}, Fig. 16c), which evidently recorded smaller amounts of finite strain, developed during the waning stages of uplift, preserving their subhorizontal axes. The dominance of high pitch values of L_D along dome flanks (independently from the orientation of S_D, Fig. 5c) is also significant, nearly perfectly reproducing the motion of rising diapirs (Cruden, 1990).

7.1.3. Changing sources: the sediment record

Age and Hf isotopic composition of most detrital zircons retrieved from the top of the Mougooderra Formation match those of magmatic zircons retrieved in the Kynea Migmatite and the Goonetarra Granodiorite (Fig. 15). In contrast, the base of this unconformable formation mainly contains 2841–2792 Ma detrital zircons (Table 1; Lu et al., 2018a) likely derived from the underlying greenstones. Such vertical distribution of detrital zircons in the Mougooderra Formation suggest therefore that doming during diapiric emplacement of the c. 2766–2749 Ma granite bodies first caused tilting and erosion of the lower greenstone succession (Fig. 16c, see also Supplementary file S1), followed by progressive unroofing of the deeper structural levels of the granite–migmatite domes, similarly to what is described in an analogous setting of the Canadian Superior Province (Lin et al., 2013).

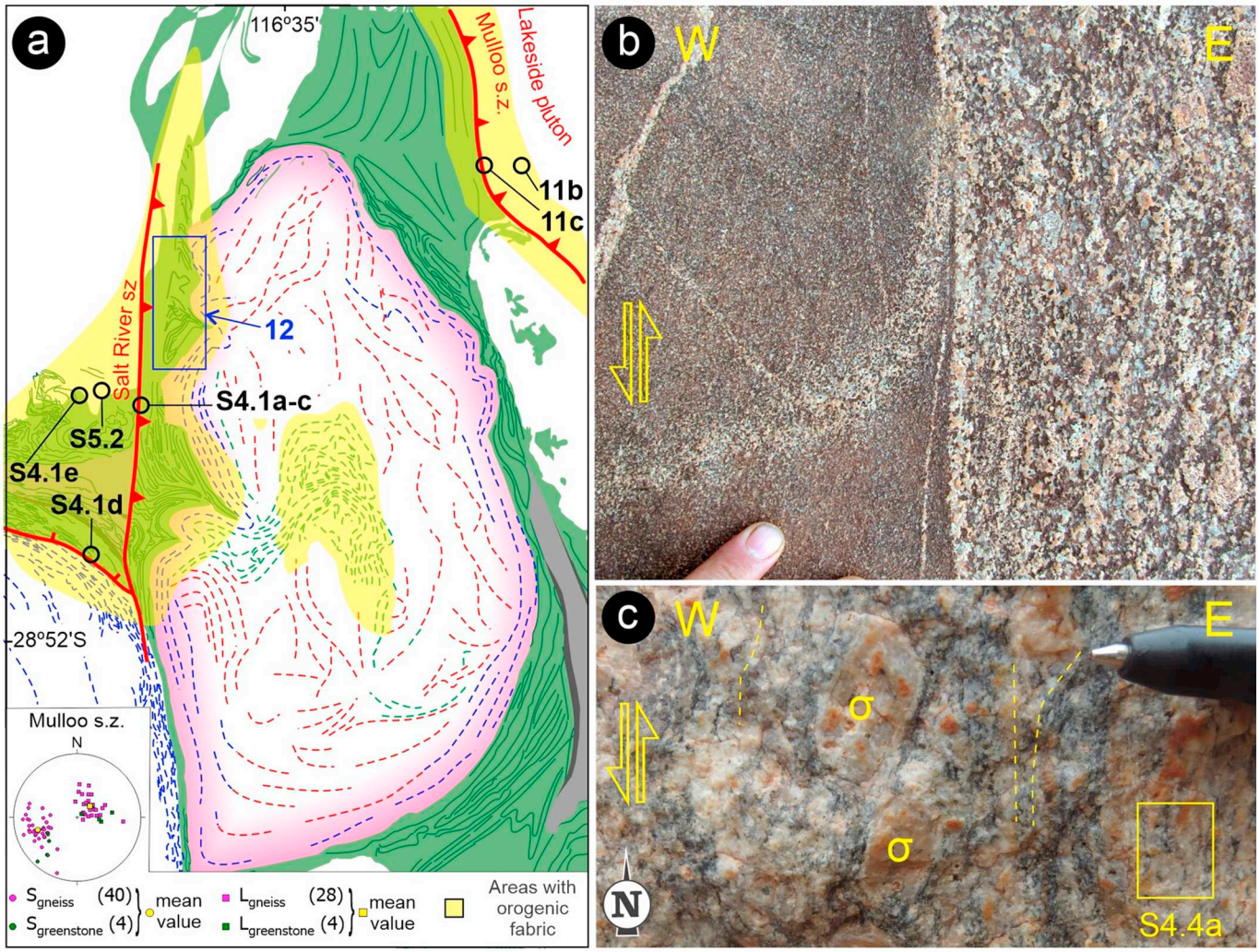

Fig. 11. The north-striking orogenic fabric. (a) Simplified map of the Yalgoo area showing the domains affected by the north-striking tectonic foliation (S_{OR}). The equal-angle plot (lower hemisphere) shows the orientation of gneissic foliation and stretching lineation measured along the Mulloo shear zone. (b) Detail from a vertical exposure showing the contact between a layered, migmatitic tonalite raft (left) and host porphyritic granite of the Lakeside pluton. The raft contains centimeter-scale leucosomes that show diffuse boundaries against host gneiss, while host granite mainly accommodated shearing through magmatic flow. (c) Vertical exposure of sheared porphyritic granite exposed along the base of the Mulloo shear zone. Sigma-type K-feldspar porphyroclasts indicate top-to-west shear sense. The corresponding microstructure is shown in Fig. S4.4a.

7.1.4. Shape of the finite strain ellipsoid

The different types of tectonites mapped here are systematically distributed throughout the region, with subvertical constriction restricted to greenstone keels (Figs. 9 and 10), in a setting otherwise regionally dominated by flattening, along the steep fabric exposed in the deeply-eroded domes (e.g. the Yalgoo dome, Figs. 4d and S3.1d), or in the domes currently exposing their flat-lying roofs (Mulgine dome, Fig. 8). Notably, the arcuate and steep axial planes of map-scale isoclinal folds in the greenstone cover wrap around the margins of each dome (Fig. 7), demonstrating that the plane of finite flattening coincides with the elliptical outline of the domes.

These distinctive structural characteristics associated with dome-and-keel architecture in the Yalgoo area have been both predicted in theoretical models and observed in areas subjected to diapirism (Collins, 1989; Van Kranendonk et al., 2004; Brun et al., 1981; Dixon, 1975; Sullivan, 2013; Talbot and Jackson, 1987; Weinberg and Podladchikov, 1994). Given the lack of a dominant foliation orientation, the lack of large-scale shear zones in the study area (Fig. 1), and the widely-preserved magmatic fabrics, the domes in the Yalgoo area can be regarded as fault-unrelated magmatic domes (Yin, 2004; Ramberg, 1981; Weinberg, 1997).

7.2. Regional-scale polydiapirism

Our regional structural mapping, complemented by geophysical data, demonstrate that the Yalgoo area exposes a gneiss dome system (≥100 by 100 km in map view, Figs. 1 and 2) composed of at least seven domes separated by narrow greenstone keels, and several

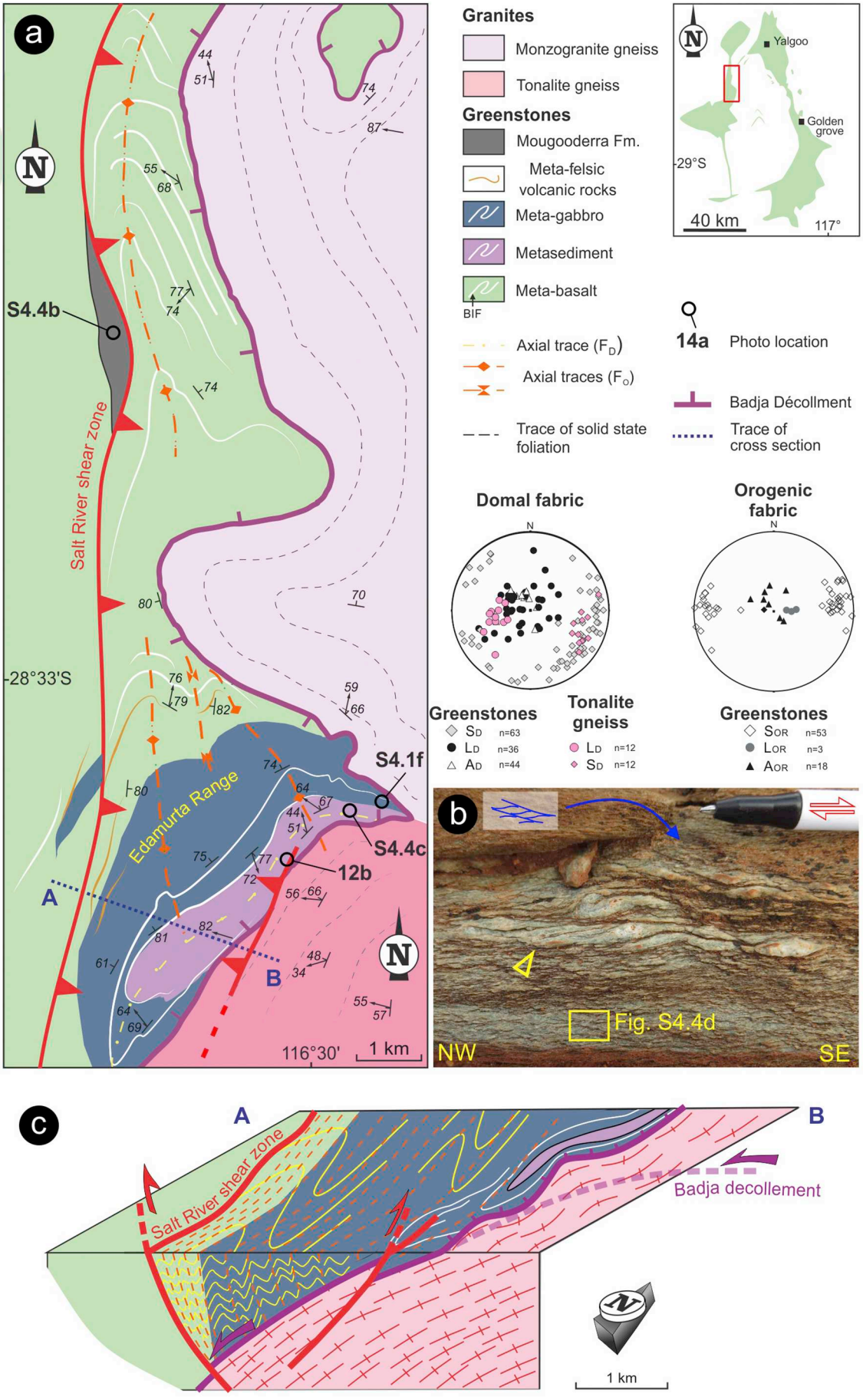

(caption on next page)

Fig. 12. (a) Geological map of the northwestern flank of the Yalgoo dome, centered on the Edamurta greenstone belt. S_D and the associated large-scale isoclinal folds are crenulated by the north-striking S_{OR}, which is subparallel to the Salt River shear zone. The west-dipping Badja décollement is locally reactivated as east-verging thrust. The two equal-angle projection plots (lower hemisphere) show the local orientation of planar and linear fabrics for both the domal and the orogenic fabrics. (b) Mylonitic pegmatite from the Edamurta Range. S–C fabric (arrowhead) and C′ shear bands (blue arrow), defined by chlorite and stretched quartzofeldspathic aggregates, indicate top-to-southeast kinematics. The corresponding microstructure is shown in Fig. S4.4d. (c) Three-dimensional cross section sketch illustrating geometry and kinematics in the Edamurta area. (For interpretation of the references to colour in this figure legend, the reader is referred to the web version of this article.)

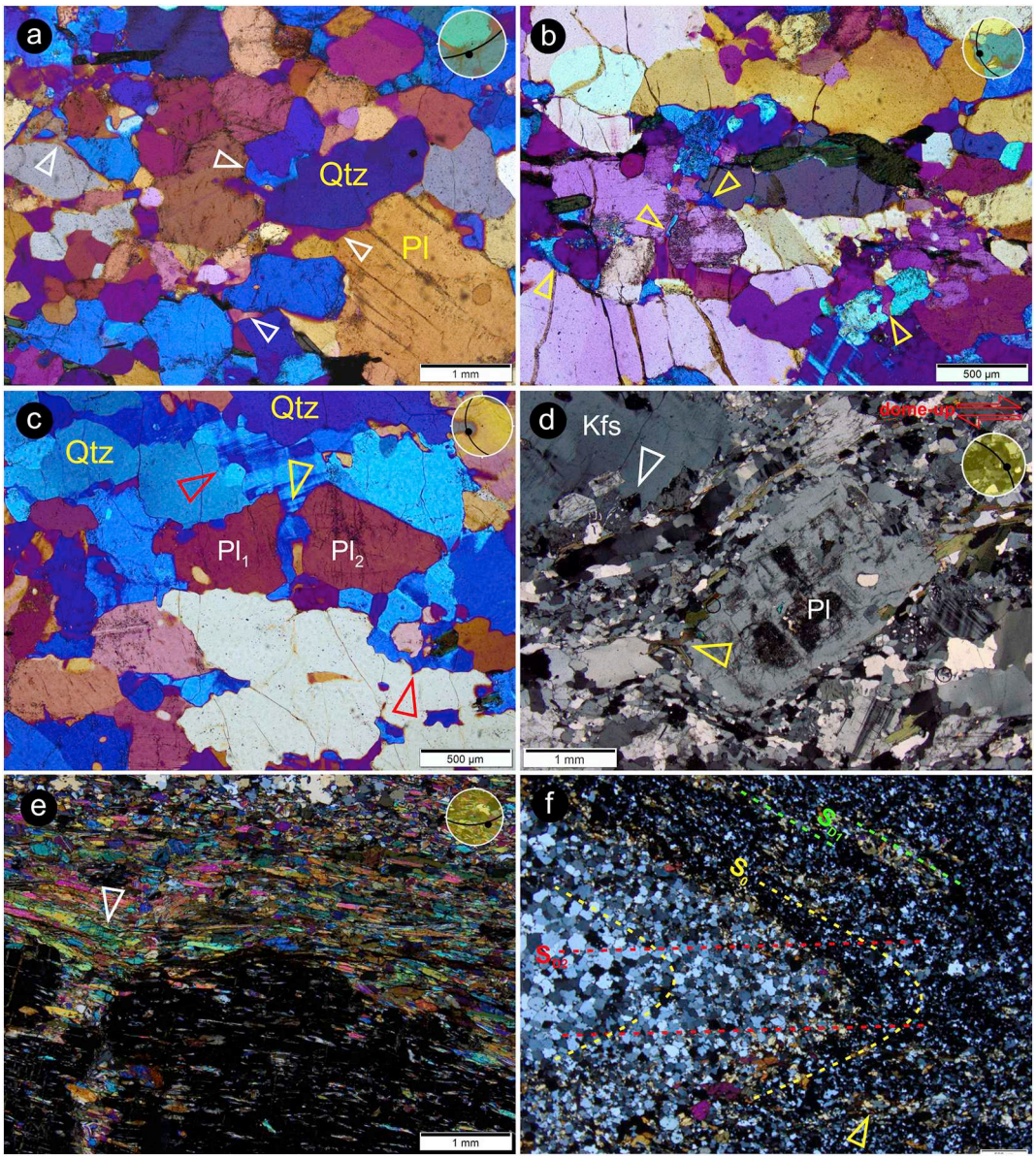

Fig. 13. Typical microstructure of the domal fabric in the Yalgoo area. All thin sections were prepared perpendicular to S_D and parallel to L_D; micrographs were taken with crossed polars. Sample numbers are mentioned where the corresponding c-axis quartz CPO is available (Fig. 14). (a) Migmatitic microstructure in Kynea Migmatite. Most plagioclase and quartz grain boundaries are embayed and are coated by thin films of K-feldspar (arrowheads), interpreted to represent former melt crystallized during shearing. Gypsum plate inserted. Sample 209689. (b) and (c) show typical microstructure of low-strain granite gneisses. (b) Thin films of K-feldspar (arrowheads) coating plagioclase–quartz grain boundaries. Gypsum plate inserted. Fractures in quartz are due to thin section preparation. (c) Microfracture in plagioclase grain (yellow arrowhead), healed by K-feldspar and quartz. Red arrowheads point to some examples of the cuspate–lobate phase boundaries between quartz and feldspars. Gypsum plate inserted. (d) High-strain porphyritic gneiss from the Gnows Nest keel area (Fig. 10b, c). Both feldspars show core-and-mantle microstructures, and K-feldspar shows strain-induced myrmekites (white arrowhead) developed along crystal faces parallel to S_D. Yellow arrowhead points to coarse-grained recrystallized plagioclase aggregates, near the margins of a plagioclase porphyroclast. Sample 155806. (e) Garnet amphibolite from the Buddadoo keel. The hornblende-rich internal foliation in garnet is concordant with the hornblende–plagioclase–quartz matrix foliation (S_D). The portion of the porphyroblast shown at left experienced boudinage, where infill is mainly represented by the matrix amphibole. Note foliation deflection (arrowhead) towards the boudinaged domain. (f) Detail from the hinge zone of millimeter-sized fold in BIF. The folded bedding (S_0) contains elongate amphibole aggregates, suggesting that it represents a composite $S_{0–D1}$ surface. A younger axial planar fabric (S_{D2}) is marked by aligned amphibole aggregates. The thin section was prepared normal to the fold axis and to L_D, accounting for the apparent lack of shape fabric in quartz aggregates. (For interpretation of the references to colour in this figure legend, the reader is referred to the web version of this article.)

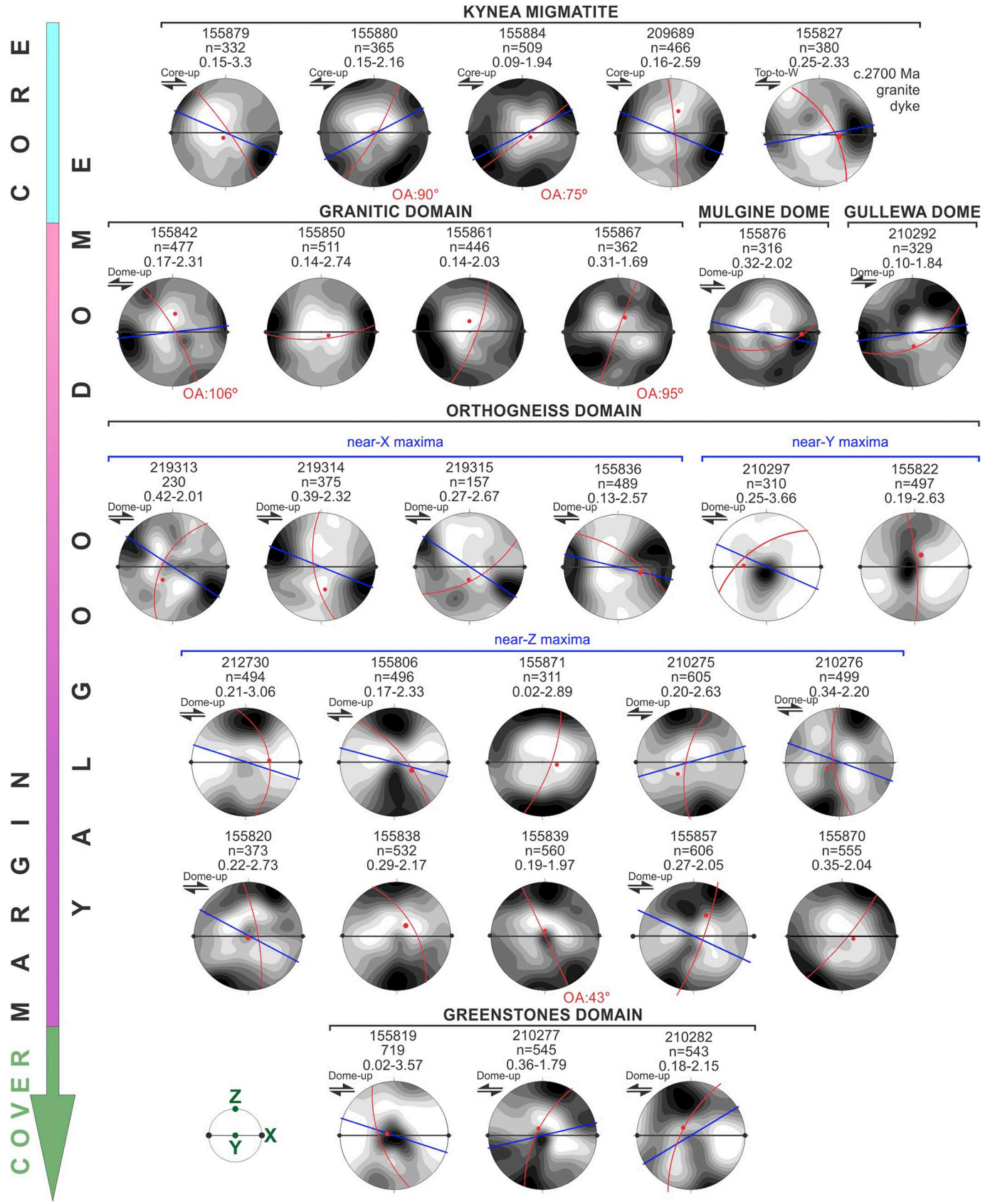

Fig. 14. Summary of quartz c-axis CPO fabrics from the Yalgoo dome area (equal-area projection plots, lower hemisphere, 1% of search area). Shear plane (blue) and sense of shear are indicated for samples showing fabric clear external symmetry. Red symbols display the orientation of foliation and lineation at each sample locality. Fig. S6.1 for sample locations. (For interpretation of the references to colour in this figure legend, the reader is referred to the web version of this article.)

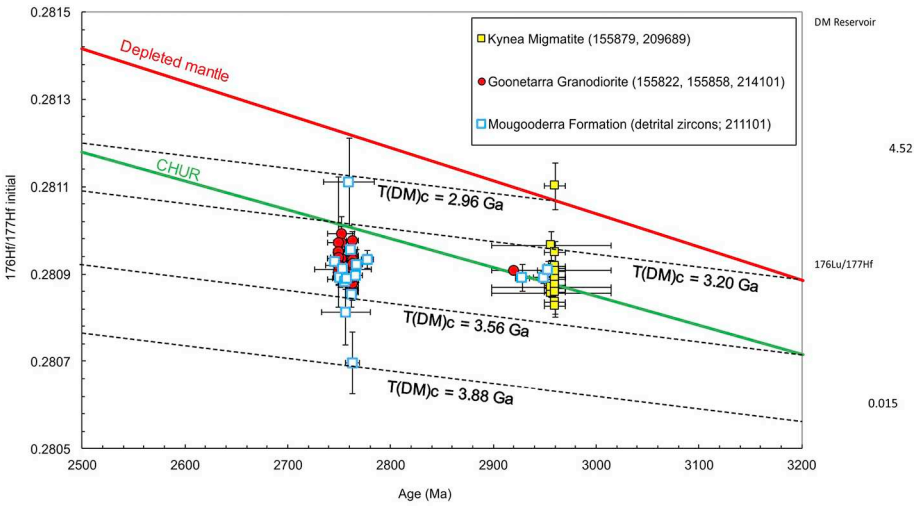

Fig. 15. Initial $^{176}Hf/^{177}Hf$ ratios versus age (Ma) plot for zircons from the granite–migmatite Yalgoo dome (from Goonetarra Granodiorite and Kynea Migmatite, respectively) and for detrital zircons from the Mougooderra Formation. Sample numbers are reported in brackets. CHUR, Chondritic Uniform Reservoir. Dashed lines represent the growth curves of average continental crust extracted from depleted mantle at c. 3.88, 3.56, 3.20 and 2.96 Ga, respectively.

subdomes within the larger domes (Figs. 2, 4c and 16c). Individual domes show a wide range of sizes (~5–50 km in average diameter), with a misorientation of their long axes (at least for the four domes that have preserved their entire outline, Figs. 2 and 7b), and exposing different structural levels. The occurrence of a single regional fabric, associated with systematic variation in the shape of the finite strain ellipsoid, and with foliation triple points near synformal keels pinched between adjacent domes, are other striking structural features of the study area.

These data indicate that the dome-and-keel architecture of the Yalgoo region resulted from multiwavelength polydiapirism (Fig. 16c; Bouhallier et al., 1995; Weinberg and Schmeling, 1992). The ≥20 Myr-long thermal anomaly generated by the multi-pulse diapirism may have favored the production of such large volumes of granitic magma, and the sequential emplacement of closely-spaced and nested diapirs, by transiently lowering the integrated viscosity of the crustal column (Weinberg, 1997). The larger domes in the Yalgoo area show average diameters > 50 km, representing some of the largest domes worldwide (compilation in Whitney et al., 2004). A process involving incremental igneous diapirism, coupled with sagduction of the greenstone cover and denudation, (Bouhallier et al., 1995; Lin et al., 2013; Stephansson, 1975) best explains the generation of very large domes whose average diameters exceed the thickness of the Neoarchean Yilgarn crust.

The total volume of granitic magma emplaced during the polydiapirism event described here cannot be accurately estimated, given the lack of three-dimensional exposure and the unknown size of three of the four large domes. An approximate volume of 75,000 km^3 of granitic material was emplaced in c. 17 Myr (Table 1) in the Yalgoo dome (volume estimation based on a 67 km of average diameter (Fig. 2), and assuming an intrusion with a perfect half-spherical shape). These results are well tuned with the data (pluton size vs. duration of assembly) compiled by Blanquat et al. (2011). For comparison, diapirism in the much smaller Naxos dome (7.5 km of average diameter) lasted c. 3 Myr (Kruckenberg et al., 2018).

The orogenic foliation discordantly overprinted the dome-and-keel architecture, reflecting episodes of east–west synorogenic shortening (Figs. 11 and 12). However, we see no evidence of either a penetrative north-oriented fabric throughout the whole region, or a reversal of the normal kinematics expressed by the high-strain zones. Important regional shortening would have also induced a rotation of the radial linear fabrics (including the long axes of all domes) towards a north-south orientation, a feature that is not observed here (Figs. 2, 5c and 7). The bulk of the structural architecture in the Yalgoo region resulted primarily from the interaction of body forces during protracted diapirism, and recorded minor, localized orogenic overprint. The regional-scale structural data presented here are consistent with recently-proposed geodynamic models (Clos et al., 2019b; Nebel et al., 2018), in which the pre-orogenic polydiapirism of the Yalgoo area essentially resulted from gravitational instabilities triggered by the long-term dynamics and magmatic activity of the convecting mantle.

Two end-member tectonic styles are recognized in Archean granite–greenstone terranes (Hickman, 2004; Condie and Benn, 2006). Dome-and-keel architecture occurs in crustal blocks whose tectonic activity was dominated by body forces, such as igneous diapirism assisted by greenstone sagduction (Bouhallier et al., 1995; Collins, 1989; Gapais et al., 2014). In contrast, Archean terranes including linear, upright fold belts are characterized by crustal-scale shear zones that are often interpreted as sutures between accreted terranes (Calvert and Ludden, 1999; Cruden et al., 2006; Myers, 1995; Van der Velden et al., 2006). These two contrasting tectonic styles are commonly inferred to reflect different tectonic settings, with craton interiors preferentially producing dome-and-keel domains, and craton margins undergoing accretion and developing elongate, ribbon-like domains with linear structures (Capitanio et al., 2019; Choukroune et al., 1997; Collins et al., 1998). A wealth of evidence also points towards a progressive, secular increase in the strength of the continental lithosphere, implying a transition from episodic-overturn/stagnant-lid regime inducing diapirism, towards modern- style plate tectonics progressively during the Neoarchean (Condie and O'Neill, 2010; Gerya, 2014; Rey and Coltice, 2008). In this context, the prominent switch in tectonic style documented here is unlikely to represent major changes in bulk lithosphere rheology, given the short time span (c. 20 Myr, between 2750 and 2730 Ma) during which such transition occurred. There is also no evidence that the Yilgarn Orogen developed along a Neoarchean craton margin, given its ~800 km width. We suggest therefore that, in a context of nearly continuous 200 Myr period of voluminous granitic magmatism, before and during the Yilgarn Orogeny, diapirism dominated in times of tectonic quiescence.

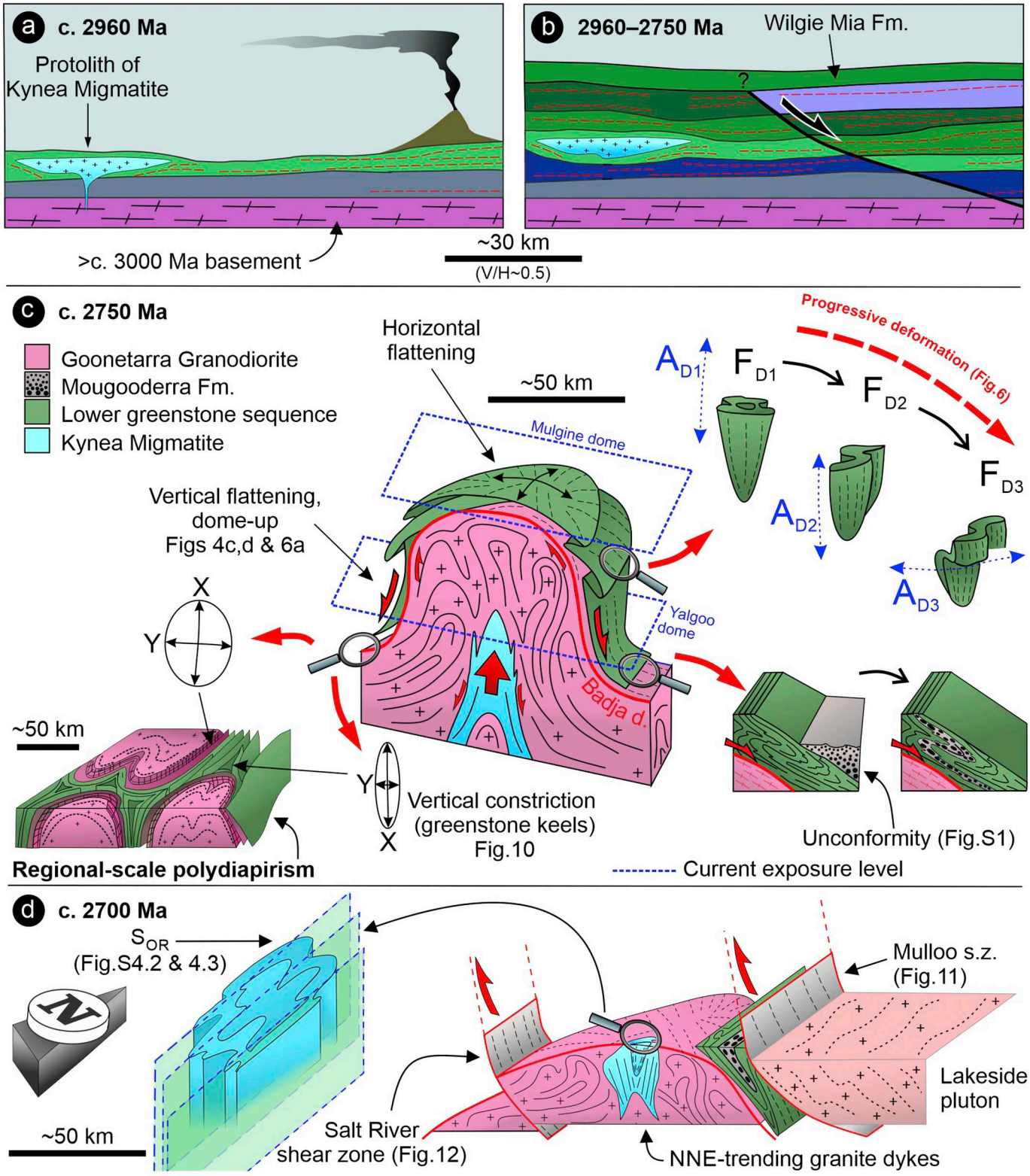

(caption on next page)

Fig. 16. Series of sketches illustrating the tectonic evolution of the Yalgoo dome. (a) Emplacement of the Kynea Migmatite into an older, continental greenstone sequence, now preserved in the core of the dome as amphibolite and BIF raft. Roughly coeval felsic volcanism is recorded by the Gossan Hill Formation, now exposed along the eastern flank of the Yalgoo dome. (b) Development of the ≥8 km-thick greenstone pile during a period likely dominated by protracted lithospheric extension. (c) Diapiric emplacement of the Goonetarra Granodiorite into the supracrustal sequence, with shear localization along the Badja décollement, which nucleated along the granite–greenstone boundary (central cartoon modified after Whitney et al., 2004). This high-strain zone mainly contains S > L tectonites, except in greenstone keels, where L > S to L tectonites developed (Fig. 10). Within the greenstone cover, progressive deformation produced: (i) syn-doming tilting of supracrustal rocks and development of a syntectonic siliciclastic sequence resting above an angular unconformity; (ii) a series of coplanar cascading folds associated with outward flow of supracrustal material and dominant subvertical stretching, with early isoclinal and sheath folds (F_{D1} and F_{D2}) refolded by upright folds (F_{D3}); (iii) shearing of the Mougooderra Formation, postdate F_{D1} folds. (d) Syn-emplacement thrusting of the Lakeside pluton along the eastern flank of the Yalgoo dome, and development of the north-striking orogenic foliation (S_{OR}), which is also well-developed along the Salt River shear zone. S_{OR} is coeval with the emplacement and shearing of the north-striking granite dykes in the core of the dome.

8. Conclusions

We outline here the tectono-magmatic evolution of the Yalgoo area, along the western margin of the Yilgarn Orogen. The oldest exposed rocks testify to the occurrence of Mesoarchean mafic and granitic magmatism (2900–2800 Ma), followed by voluminous pulses of granitic magmatism in the c. 2766–2747 Ma time span. Magma delivery occurred through polydiapirism, associated with shear localization along the roof of the resulting domes, and triggering uplift, erosion and outward flow of the supracrustal sequence. The interference between adjacent and roughly-coeval domes, accommodated by the sagduction of synformal greenstone keels, produced the characteristic dome-and-keel regional architecture, during a period of regional-scale tectonic quiescence that preceded the c. 2730 Ma onset of the Neoarchean Yilgarn Orogeny.

Supplementary data to this article can be found online at https://doi.org/10.1016/j.tecto.2020.228375.

CRediT authorship contribution statement

I. Zibra: Conceptualization, Data curation, Formal analysis, Supervision, Validation, Visualization, Writing - original draft, Writing - review & editing. **Y. Lu**: Data curation, Writing - review & editing. **F. Clos**: Data curation, Writing - review & editing. **R.F. Weinberg**: Data curation, Writing - review & editing. **M. Peternell**: Data curation, Writing - review & editing. **M.T.D. Wingate**: Data curation, Writing - review & editing. **M. Prause**: Data curation, Writing - review & editing. **M. Schiller**: Data curation, Writing - review & editing. **R. Tilhac**: Data curation, Writing - review & editing.

Declaration of competing interest

All authors included in this contribution declare that none of them has financial and personal relationships with other people or organizations that could inappropriately influence (bias) their work.

Acknowledgements

Constructive reviews from Christian Teyssier and Martin Van Kranendonk are greatly appreciated. Likewise, supportive comments by Bill Collins and Patrice Rey, on an earlier version of the manuscript, helped improving the clarity of this contribution. Students James N. Caudery, Michael J. Fenwick and Aaron Tomkins contributed with mapping and sample preparation. The staff of the GSWA laboratory prepared the samples for geochronology and geochemistry; their accurate work is greatly appreciated. John Brett prepared the geophysical map shown in Figs. 4 and 7. The Hf analytical data were obtained using instrumentation funded by DEST Systemic Infrastructure Grants, ARC LIEF, NCRIS/Auscope industry partners and Macquarie University. This is contribution 1425 from the ARC Centre of Excellence for Core to Crust Fluid Systems (http://www.ccfs.mq.edu.au) and 1367 in the GEMOC Key Centre (http://www.gemoc.mq.edu.au) Additional data sets supporting our conclusions are included in the Supporting Information.

References[1]

Blanquat, M. de Saint, Horsman, E., Habert, G., Morgan, S., Vanderhaeghe, O., Law, R., Tikoff, B., 2011. Multiscale magmatic cyclicity, duration of pluton construction, and the paradoxical relationship between tectonism and plutonism in continental arcs. Tectonophysics 500, 20–33. https://doi.org/10.1016/j.tecto.2009.12.009.

Bouhallier, H., Chardon, D., Choukroune, P., 1995. Strain patterns in Archaean dome-and-basin structures: the Dharwar craton (Karnataka, South India). Earth Planet. Sci. Lett. 135, 57–75. https://doi.org/10.1016/0012-821X(95)00144-2.

Bouvier, A., Vervoort, J.D., Patchett, P.J., 2008. The Lu-Hf and Sm-Nd isotopic composition of CHUR: constraints from unequilibrated chondrites and implications for the bulk composition of terrestrial planets. Earth Planet. Sci. Lett. 273, 48–57. https://doi.org/10.1016/j.epsl.2008.06.010.

Brun, J.P., Gapais, D., Le Theoff, B., 1981. The mantled gneiss domes of Kuopio (Finland): interfering diapirs. Tectonophysics 74, 283–304.

Calvert, A.J.A., Ludden, J.N., 1999. Archean continental assembly in the southeastern superior province of Canada. Tectonics 18, 412–429. https://doi.org/10.1029/1999TC900006.

Capitanio, F.A., Nebel, O., Cawood, P.A., Weinberg, R.F., Clos, F., 2019. Lithosphere differentiation in the early Earth controls Archean tectonics. Earth Planet. Sci. Lett. 525, 115755. https://doi.org/10.1016/j.epsl.2019.115755.

Cassidy, K., Champion, D., McNaughton, N., Whitaker, A., Bastrakova, I., Budd, A., 2002. Characterisation and Metallogenic Significance of Archaean Granitoids of the Yilgarn Craton, Western Australia. Minerals and Energy Research Institute of Western Australia (MERIWA) Project no. M281/AMIRA Project no. 482 (unpublished Report No. 222).

Cassidy, K., Champion, D., Krapez, B., Barley, M., 2006. A revised geological framework for the Yilgarn Craton, Western Australia., Geological Survey of Western Australia. Record 8 (8).

Chardon, D., Choukroune, P., Jayananda, M., 1996. Strain patterns, décollement and incipient sagducted greenstone terrains in the Archaean Dharwar craton (south India). J. Struct. Geol. 18, 991–1004. https://doi.org/10.1016/0191-8141(96)00031-4.

Chen, S., Riganti, A., Wyche, S., Greenfield, J., 2003. Lithostratigraphy and tectonic evolution of contrasting greenstone successions in the central Yilgarn Craton, Western Australia. Precambrian Res. 127, 249–266.

Choukroune, P., Ludden, J.N., Chardon, D., Calvert, A.J., Bouhallier, H., 1997. Archaean crustal growth and tectonic processes: a comparison of the Superior Province, Canada and the Dharwar Craton, India. Geol. Soc. London, Spec. Publ. 121, 63–98. https://doi.org/10.1144/GSL.SP.1997.121.01.04.

Clos, F., Weinberg, R., Zibra, I., Fenwick, M., 2019a. Archean diapirism recorded by vertical sheath folds in the core of the Yalgoo Dome, Yilgarn Craton. Precambrian Res. 320, 391–402. https://doi.org/10.1016/j.precamres.2018.11.010.

Clos, F., Weinberg, R., Zibra, I., Schwindinger, M., 2019b. Magmatic and anatectic history of a large Archean diapir: insights from the migmatitic core of the Yalgoo Dome, Yilgarn Craton. Lithos. https://doi.org/10.1016/j.lithos.2019.04.012.

Collins, W., 1989. Polydiapirism of the Archean Mount Edgar Batholith, Pilbara Block, Western Australia. Precambrian Res. 43, 41–62.

Collins, W., Van Kranendonk, M., Teyssier, C., 1998. Partial convective overturn of Archaean crust in the east Pilbara Craton, Western Australia: driving mechanisms and tectonic implications. J. Struct. Geol. 20, 1405–1424. https://doi.org/10.1016/S0191-8141(98)00073-X.

Condie, K.C., Benn, K., 2006. Archean geodynamics: similar to or different from modern geodynamics? Archean Geodyn. Environ. 47–59.

Condie, K.C., O'Neill, C., 2010. The Archean-Proterozoic boundary: 500 My of tectonic transition in earth history. Am. J. Sci. 310, 775–790. https://doi.org/10.2475/09.2010.01.

Cruden, A.R., 1988. Deformation around a rising diapir modeled by creeping flow past a

[1] References cited in Table 1 and in Supporting Information files (reported here below just to allow insertion in the list, which is automatically generated by the Mendeley citation software): Bouvier et al. (2008); De Bievre and Taylor (1993); Griffin et al. (2000); Griffin et al. (2002); Pearson et al. (2008); Söderlund et al. (2004); Lu et al. (2016a); Lu et al. (2016b, 2018b); Wingate et al. (2015a, 2018); Lu et al. (2017a, 2017b); Wingate et al. (2015b); Lu et al. (2017c); Wiedenbeck and Watkins (1993); Cassidy et al. (2002); Lu et al. (2020a, 2020b).

sphere. Tectonics 7, 1091–1101. https://doi.org/10.1029/TC007i005p01091.
Cruden, A., 1990. Flow and fabric development during the diapiric rise of magma. J. Geol. 98, 681–698.
Cruden, A., Nasseri, M., Pysklywec, R., 2006. Surface topography and internal strain variation in wide hot orogens from three-dimensional analogue and two-dimensional numerical vice models. Geol. Soc. London, Spec. 253, 79–104.
De Bievre, P., Taylor, P.D.P., 1993. Table of the isotopic compositions of the elements. Int. J. Mass Spectrom. Ion Process. 123, 149–166.
Dixon, J.M., 1975. Finite strain and progressive deformation in models of diapiric structures. Tectonophysics 28, 89–124. https://doi.org/10.1016/0040-1951(75)90060-8.
Dixon, J.M., Summers, J.M., 1983. Patterns of total and incremental strain in subsiding troughs: experimental centrifuged models of inter- diapir synclines. Can. J. Earth Sci. 20, 1843–1861. https://doi.org/10.1139/e83-175.
Drummond, B.J., Goleby, B.R., Swager, C.P., 2000. Crustal signature of Late Archaean tectonic episodes in the Yilgarn craton, Western Australia: evidence from deep seismic sounding. Tectonophysics 329, 193–221. https://doi.org/10.1016/S0040-1951(00)00196-7.
Eskola, P.E., 1948. The problem of mantled gneiss domes. Q. J. Geol. Soc. 104, 461–476. https://doi.org/10.1144/GSL.JGS.1948.104.01-04.21.
Fenwick, M.J., 2014. Structural evolution of the Yalgoo Dome, Yilgarn Craton, Western Australia: a core perspective. In: Geological Survey of Western Australia, Record 2014/16.
François, C., Philippot, P., Rey, P., Rubatto, D., 2014. Burial and exhumation during Archean sagduction in the east Pilbara granite-greenstone terrane. Earth Planet. Sci. Lett. 396, 235–251.
Gapais, D., Jaguin, J., Cagnard, F., Boulvais, P., 2014. Pop-down tectonics, fluid channelling and ore deposits within ancient hot orogens. Tectonophysics 618, 102–106. https://doi.org/10.1016/j.tecto.2014.01.027.
Gerya, T., 2014. Precambrian geodynamics: concepts and models. Gondwana Res. 25, 442–463.
Gower, R.J.W., Simpson, C., 1992. Phase boundary mobility in naturally deformed, high-grade quartzofeldspathic rocks: evidence for diffusional creep. J. Struct. Geol. 14, 301–313. https://doi.org/10.1016/0191-8141(92)90088-E.
Griffin, W.L., Pearson, N.J., Belousova, E., Jackson, S.E., Van Achterbergh, E., O'Reilly, S.Y., Shee, S.R., 2000. The Hf isotope composition of cratonic mantle: LAM-MC-ICPMS analysis of zircon megacrysts in kimberlites. Geochim. Cosmochim. Acta 64, 133–147. https://doi.org/10.1016/S0016-7037(99)00343-9.
Griffin, W.L., Wang, X., Jackson, S.E., Pearson, N.J., O'Reilly, S.Y., Xu, X., Zhou, X., 2002. Zircon chemistry and magma mixing, SE China: in-situ analysis of Hf isotopes, Tonglu and Pingtan igneous complexes. Lithos 61, 237–269. https://doi.org/10.1016/S0024-4937(02)00082-8.
Hammes, D.M., Peternell, M., 2016. FAME: software for analysing rock microstructures. Comput. Geosci. 90, 24–33.
Hickman, A.H., 2004. Two contrasting granite-greenstone terranes in the Pilbara Craton, Australia: Evidence for vertical and horizontal tectonic regimes prior to 2900 Ma. In: Precambrian Research, pp. 153–172. https://doi.org/10.1016/j.precamres.2003.12.009.
Ivanic, T., Van Kranendonk, M.J., Kirkland, C.L., Wyche, S., Wingate, M.T.D., Belousova, E.A., 2012. Zircon Lu-Hf isotopes and granite geochemistry of the Murchison Domain of the Yilgarn Craton: Evidence for reworking of Eoarchean crust during Meso-Neoarchean plume-driven magmatism. Lithos 148, 112–127. https://doi.org/10.1016/j.lithos.2012.06.006.
Ivanic, T., Li, J., Meng, Y., Guo, L., Yu, J., Chen, S.F., Wyche, S., Zibra, I., 2015. Yalgoo, WA Sheet 2241: Geological Survey of Western Australia, 1:100 000 Geological Series.
Jackson, M.P.A., Talbot, C.J., 1989. Anatomy of mushroom-shaped diapirs. J. Struct. Geol. 11, 211–230. https://doi.org/10.1016/0191-8141(89)90044-8.
Johnson, T.E., Brown, M., Gardiner, N.J., Kirkland, C.L., Smithies, R.H., 2017. Earth's first stable continents did not form by subduction. Nature 543, 239–242. https://doi.org/10.1038/nature21383.
Klein, C., 2005. Some Precambrian banded iron-formations (BIFs) from around the world: their age, geologic setting, mineralogy, metamorphism, geochemistry, and origin. Am. Mineral. 90, 1473–1499.
Kruckenberg, S.C., Vanderhaeghe, O., Ferré, E.C., Teyssier, C., Whitney, D.L., 2011. Flow of partially molten crust and the internal dynamics of a migmatite dome, Naxos, Greece. Tectonics 30https://doi.org/10.1029/2010TC002751. (n/a-n/a).
Kruckenberg, S., Martin, L., Gerbault, M., Vanderhaeghe, O., Deloule, E., Duchêne, S., 2018. Crustal-scale convection and diapiric upwelling of a partially molten orogenic root (Naxos dome, Greece). Tectonophysics 746, 459–469. https://doi.org/10.1016/j.tecto.2018.03.007.
Kruhl, J.H., 1996. Prism- and basal-plane parallel subgrain boundaries in quartz: A microstructural geothermobarometer. J. Metamorph. Geol. 14, 581–589.
Law, R.D., 2014. Deformation thermometry based on quartz c-axis fabrics and recrystallization microstructures: a review. J. Struct. Geol. 66, 129–161. https://doi.org/10.1016/j.jsg.2014.05.023.
Lin, S., Parks, J., Heaman, L.M., Simonetti, A., Corkery, M.T., 2013. Diapirism and sagduction as a mechanism for deposition and burial of "Timiskaming-type" sedimentary sequences, Superior Province: evidence from detrital zircon geochronology and implications for the Borden Lake conglomerate in the exposed middle to lower. Precambrian Res 238, 148–157. https://doi.org/10.1016/j.precamres.2013.09.012.
Lister, G., 1977. Discussion: crossed-girdle c-axis fabrics in quartzites plastically deformed by plane strain and progressive simple shear. Tectonophysics 39, 51–54.
Lister, G.S., Davis, G.A., 1989. The origin of metamorphic core complexes and detachment faults formed during Tertiary continental extension in the northern Colorado River region, U.S.A. J. Struct. Geol. 11, 65–94. https://doi.org/10.1016/0191-8141(89)90036-9.
Little, T.A., Hacker, B.R., Gordon, S.M., Baldwin, S.L., Fitzgerald, P.G., Ellis, S., Korchinski, M., 2011. Diapiric exhumation of Earth's youngest (UHP) eclogites in the gneiss domes of the D'Entrecasteaux Islands, Papua New Guinea. Tectonophysics 510, 39–68. https://doi.org/10.1016/j.tecto.2011.06.006.
Lu, Yongjun, Wingate, M.T.D., Kirkland, C., Ivanic, T., 2016. 211101: Volcaniclastic Mudstone, Wadgingarra Hill; Geochronology Record 1337. Geological Survey of Western Australia.
Lu, Y., Wingate, M.T.D., Kirkland, C., Ivanic, T., 2016a. 198294: metamorphosed Quartz Diorite, Mugs Luck Mine; Geochronology Record 1332: Geological Survey of Western Australia.
Lu, Y., Wingate, M.T.D., Kirkland, C., Ivanic, T., 2016b. 198298: Metadacite, Wadgingarra Well; Geochronology Record 1334: Geological Survey of Western Australia.
Lu, Y., Wingate, M.T.D., Kirkland, C., Zibra, I., 2017a. 214101: monzogranite gneiss, Picketer Well. In: Geochronology Record 1466. Geological Survey of Western Australia.
Lu, Y., Wingate, M.T.D., Kirkland, C., Zibra, I., 2017b. 155858: metamonzogranite, Mac Well. In: Geochronology Record 1393. Geological Survey of Western Australia.
Lu, Y., Wingate, M.T.D., Kirkland, C., Zibra, I., 2017c. 209689: Metatonalite, Wooley Spring; Geochronology Record 1463: Geological Survey of Western Australia.
Lu, Y., Wingate, M.T.D., Ivanic, T.J., 2018a. 198296: Quartz Sandstone, Warriedar Hill; Geochronology Record 1501: Geological Survey of Western Australia.
Lu, Y., Wingate, M.T.D., Kirkland, C., 2018b. 203701: metadacite, Cattle Well. In: Geochronology Record 1495. Geological Survey of Western Australia.
Lu, Y., Wingate, M., Zibra, I., 2020a. 155843: tonalite gneiss, Windagalcudga Well. In: Geochronology Record 1646. Geological Survey of Western Australia.
Lu, Y., Wingate, M., Zibra, I., 2020b. 155875: metagranodiorite, Mulga Well. In: Geochronology Record 1647. Geological Survey of Western Australia.
Mainprice, D., Bouchez, J.J.L., Blumenfeld, P., Tubià, J.M.J., 1986. Dominant c slip in naturally deformed quartz: implications for dramatic plastic softening at high temperature. Geology 14, 819–822 doi:10.1130/0091-7613(1986)14 < 819:DCSIND > 2.0.CO;2.
Mareschal, J.-C., West, G.F., 1980. A model for Archean tectonism. Part 2. Numerical models of vertical tectonism in greenstone belts. Can. J Earth Sci. 17, 60–71. https://doi.org/10.1139/e80-006.
Morris, P.A., Riganti, A., Chen, S.F., 2007. Evaluating the provenance of Archean sedimentary rocks of the Diemals Formation (central Yilgarn Craton) using whole-rock chemistry and precise U-Pb zircon chronology. Aust. J. Earth Sci. 54, 1123–1136.
Myers, J.S., 1995. The generation and assembly of an Archaean supercontinent: evidence from the Yilgarn craton, Western Australia. Geol. Soc. London, Spec. Publ. 95, 143–154. https://doi.org/10.1144/GSL.SP.1995.095.01.09.
Myers, J.S., Watkins, K.P., 1985. Origin of granite-greenstone patterns, Yilgarn Block, Western Australia. Geology 13, 778–780.
Nebel, O., Capitanio, F.A., Moyen, J.-F.F., Weinberg, R.F., Clos, F., Nebel-Jacobsen, Y.J., Cawood, P.A., 2018. When crust comes of age: on the chemical evolution of Archaean, felsic continental crust by crustal drip tectonics. Philosophical Transactions of the Royal Society A: Mathematical, Physical and Engineering Sciences 20180103. https://doi.org/10.1098/rsta.2018.0103.
Passchier, C., Trouw, R.A.J., 2005. Microtectonics, second ed. Springer, Berlin, Heidelberg, New York. Springer, Berlin.
Pearson, N.J., Griffin, W.L., O'Reilly, S.Y., 2008. Mass Fractionation Correction in Laser Ablation Multiple-collector ICP-MS: Implications for Overlap Corrections and Precise and Accurate In Situ Isotope Ratio Measurement.
Peternell, M., Hasalová, P., Wilson, C.J.L., Piazolo, S., Schulmann, K., 2010. Evaluating quartz crystallographic preferred orientations and the role of deformation partitioning using EBSD and fabric analyser techniques. J. Struct. Geol. 32, 803–817.
Ramberg, H., 1972. Theoretical models of density stratification and diapirism in the Earth. J. Geo. Res. 77, 877–889. https://doi.org/10.1029/JB077i005p00877.
Ramberg, H., 1981. The role of gravity in orogenic belts. Geol. Soc. London, Spec. Publ. 9, 125–140. https://doi.org/10.1144/GSL.SP.1981.009.01.11.
Ramsay, J.G., 1967. Folding and Fracturing of Rocks. McGraw-Hill, New York. https://doi.org/10.1126/science.160.3826.410.
Rey, P.F., Coltice, N., 2008. Neoarchean lithospheric strengthening and the coupling of Earth's geochemical reservoirs. Geology 36, 635. https://doi.org/10.1130/G25031A.1.
Rosenberg, C., Stünitz, H., 2003. Deformation and recrystallization of plagioclase along a temperature gradient: an example from the Bergell tonalite. J. Struct. Geol. 25, 389–408.
Sawyer, E.W., 1999. Criteria for the recognition of partial melting. Phys. Chem. Earth, Part A Solid Earth Geod. 24, 269–279. https://doi.org/10.1016/S1464-1895(99)00029-0.
Sawyer, E.W., 2008. Atlas of migmatites. The Canadian Mineralogist, Special publication 9. NRC Research Press, Ottawa, Ontario, Canada.
Simpson, C., Wintsch, R.P., 1989. Evidence for deformation-induced K-feldspar replacement by myrmekite. J. Metamorph. Geol. 7, 261–275.
Smithies, R.H., 2000. The Archaean tonalite–trondhjemite–granodiorite (TTG) series is not an analogue of Cenozoic adakite. Earth Planet. Sci. Lett. 182, 115–125.
Smithies, R., Ivanic, T.J., Lowrey, J.R., Morris, P.A., Barnes, S.J., Wyche, S., Lu, Y.-J., 2018. Two distinct origins for Archean greenstone belts. Earth Planet. Sci. Lett. 487, 106–116. https://doi.org/10.1016/j.epsl.2018.01.034.
Söderlund, U., Patchett, P.J., Vervoort, J.D., Isachsen, C.E., 2004. The176Lu decay constant determined by Lu-Hf and U-Pb isotope systematics of Precambrian mafic intrusions. Earth Planet. Sci. Lett. 219, 311–324. https://doi.org/10.1016/S0012-821X(04)00012-3.
Stephansson, O., 1975. Polydiapirism of granitic rocks in the Svecofennian of Central Sweden. Precambrian Res. 2, 189–214. https://doi.org/10.1016/0301-9268(75)

90003-0.
Stipp, M., Stünitz, H., Heilbronner, R., Schmid, S.M., 2002. The eastern Tonale fault zone: a 'natural laboratory' for crystal plastic deformation of quartz over a temperature range from 250 to 700 C. J. Struct. Geol. 24, 1861–1884.
Sullivan, W.A., 2013. L tectonites. J. Struct. Geol. 50, 161–175. https://doi.org/10.1016/j.jsg.2012.01.022.
Talbot, C.J., Jackson, M.P.A., 1987. Internal kinematics of salt diapirs. Am. Assoc. Pet. Geol. Bull. 71, 1068–1093.
Teyssier, C., Whitney, D.L., 2002. Gneiss domes and orogeny. Geology 30, 1139 doi:10.1130/0091-7613(2002)030 < 1139:GDAO > 2.0.CO;2.
Van der Velden, A.J., Cook, F.A., Drummond, B.J., Goleby, B.R., 2006. Reflections of the Neoarchean: a global perspective. In: Archean Geodynamics and Environments, pp. 255–265. https://doi.org/10.1029/164GM16.
Van Kranendonk, M., Collins, W., Hickman, A., 2004. Critical tests of vertical vs. horizontal tectonic models for the Archaean East Pilbara granite–greenstone terrane, Pilbara craton, western Australia. Precambrian Res. 131, 173–211.
Van Kranendonk, M., Ivanic, T.J., Wingate, M.T.D., Kirkland, C.L., Wyche, S., 2013. Long-lived, autochthonous development of the Archean Murchison Domain, and implications for Yilgarn Craton tectonics. Precambrian Res. 229, 49–92.
Vanderhaeghe, O., 2004. Structural development of the Naxos migmatite dome. In: Special Paper 380: Gneiss Domes in Orogeny. Geological Society of America, pp. 211–227. https://doi.org/10.1130/0-8137-2380-9.211.
Vanderhaeghe, O., Teyssier, C., Wysoczanski, R., 2011. Structural and geochronological constraints on the role of partial melting during the formation of the Shuswap metamorphic core complex at the latitude of the Thor-Odin dome, British Columbia. Can. J. Earth Sci. 36, 917–943. https://doi.org/10.1139/e99-023.
Vearncombe, J., 1998. Shear zones, fault networks, and Archean gold. Geology 26, 855–858.
Watkins, K., Hickman, A., 1990. Geological Evolution and Mineralization of the Murchison Province, Western Australia.
Weinberg, R.F., 1997. Diapir-driven crustal convection: decompression melting, renewal of the magma source and the origin of nested plutons. Tectonophysics 271, 217–229. https://doi.org/10.1016/S0040-1951(96)00269-7.
Weinberg, R.F., Podladchikov, Y., 1994. Diapiric ascent of magmas through power law crust and mantle. J. Geophys. Res. Solid Earth 99, 9543–9559. https://doi.org/10.1029/93JB03461.
Weinberg, R.F., Podladchikov, Y.Y., 1995. The rise of solid-state diapirs. J. Struct. Geol. 17, 1183–1195.
Weinberg, R., Schmeling, H., 1992. Polydiapirs: multiwavelength gravity structures. J. Struct. Geol. 14, 425–436. https://doi.org/10.1016/0191-8141(92)90103-4.
Whitney, D.L., Teyssier, C., Vanderhaeghe, O., 2004. Gneiss domes and crustal flow. Geol. Soc. Am. Spec. Pap 1–19. https://doi.org/10.1130/0–8137–2380-9.15.
Wiedenbeck, M., Watkins, K.P., 1993. A time scale for granitoid emplacement in the Archean Murchison Province, Western Australia, by single zircon geochronology. Precambrian Res. 61, 1–26. https://doi.org/10.1016/0301-9268(93)90055-7.
Wilde, S.A., Middleton, M.F., Evans, B.J., 1996. Terrane accretion in the southwestern Yilgarn Craton: evidence from a deep seismic crustal profile. Precambrian Res. 78, 179–196.
Wilson, C.J.L., Russell-Head, D.S., Kunze, K., Viola, G., 2007. The analysis of quartz c-axis fabrics using a modified optical microscope. J. Microsc. 227, 30–41. https://doi.org/10.1111/j.1365-2818.2007.01784.x.
Wingate, M.T.D., Kirkland, C., Zibra, I., Wyche, S., 2015a. 155822: monzogranite gneiss, Three Mile Well. In: Geochronology Record 1247. Geological Survey of Western Australia.
Wingate, M.T.D., Kirkland, C.L., Zibra, I., 2015b. 155879: Granodiorite Gneiss, Toben Bore; Geochronology Record 1245: Geological Survey of Western Australia.
Wingate, M.T.D., Lu, Y., Ivanic, T., 2018. 207628: Altered Metamonzogranite, Mulgine Hill; Geochronology Record 1460: Geological Survey of Western Australia.
Wyche, S., Kirkland, C.L., Riganti, A., Pawley, M.J., Belousova, E., Wingate, M.T.D., 2012. Isotopic constraints on stratigraphy in the central and eastern Yilgarn Craton, Western Australia. Aust. J. Earth 59, 657–670. https://doi.org/10.1080/08120099.2012.697677.
Yin, A., 2004. Gneiss domes and gneiss dome systems. In: Special Paper 380: Gneiss Domes in Orogeny. Geological Society of America, pp. 1–14. https://doi.org/10.1130/0-8137-2380-9.1.
Zeh, A., Gerdes, A., Klemd, R., Barton Jr., J.M., 2008. U-Pb and Lu-Hf isotope record of detrital zircon grains from the Limpopo Belt–evidence for crustal recycling at the Hadean to early-Archean transition. Geochim. Cosmochim. Acta 72, 5304–5329.
Zibra, I., 2012. Syndeformational granite crystallisation along the Mount Magnet Greenstone Belt, Yilgarn Craton: evidence of large-scale magma-driven strain localisation during Neoarchean times. Aust. J. Earth Sci. 59, 793–806. https://doi.org/10.1080/08120099.2012.684887.
Zibra, I., Kruhl, J., Montanini, A., Tribuzio, R., 2012. Shearing of magma along a high-grade shear zone: evolution of microstructures during the transition from magmatic to solid-state flow. J. Struct. Geol. 37, 150–160. https://doi.org/10.1016/j.jsg.2012.01.011.
Zibra, I., Gessner, K., Smithies, H., Peternell, M., 2014. On shearing, magmatism and regional deformation in Neoarchean granite-greenstone systems: INSIGHTS from the Yilgarn Craton. J. Struct. Geol. https://doi.org/10.1016/j.jsg.2013.11.010.
Zibra, I., Ivanic, T.J., Chen, S.F., Clos, F., 2016. Badja, WA Sheet 2240: Geological Survey of Western Australia. In: 1:100 000 Geological Series, Available at: http://dmpbookshop.eruditetechnologies.com.au/product/badja-wa-sheet-2240.do.Perth.
Zibra, I., Clos, F., Weinberg, R., Peternell, M., 2017. The ~2730 Ma onset of the Neoarchean Yilgarn Orogeny. Tectonics 36, 1787–1813. https://doi.org/10.1002/2017TC004562.